

Review



Cite this article: Galenko PK, Alexandrov DV, Titova EA. 2018 The boundary integral theory for slow and rapid curved solid/liquid interfaces propagating into binary systems. *Phil. Trans. R. Soc. A* **376**: 20170218. <http://dx.doi.org/10.1098/rsta.2017.0218>

Accepted: 18 September 2017

One contribution of 16 to a theme issue 'From atomistic interfaces to dendritic patterns'.

Subject Areas:

mathematical modelling, mathematical physics, solid-state physics

Keywords:

boundary integral method, phase transitions, propagation of curved interfaces, crystal growth, parabolic and hyperbolic transport equations, Ivantsov and Horvay–Cahn solutions

Author for correspondence:

Peter K. Galenko
e-mail: peter.galenko@uni-jena.de

The boundary integral theory for slow and rapid curved solid/liquid interfaces propagating into binary systems

Peter K. Galenko¹, Dmitri V. Alexandrov² and Ekaterina A. Titova²

¹Physikalisch-Astronomische Fakultät, Friedrich-Schiller-Universität Jena, 07743 Jena, Germany

²Department of Theoretical and Mathematical Physics, Laboratory of Multi-Scale Mathematical Modeling, Ural Federal University, Ekaterinburg 620000, Russian Federation

PKG, 0000-0003-2941-7742; DVA, 0000-0002-6628-745X

The boundary integral method for propagating solid/liquid interfaces is detailed with allowance for the thermo-solutal Stefan-type models. Two types of mass transfer mechanisms corresponding to the local equilibrium (parabolic-type equation) and local non-equilibrium (hyperbolic-type equation) solidification conditions are considered. A unified integro-differential equation for the curved interface is derived. This equation contains the steady-state conditions of solidification as a special case. The boundary integral analysis demonstrates how to derive the quasi-stationary Ivantsov and Horvay–Cahn solutions that, respectively, define the paraboloidal and elliptical crystal shapes. In the limit of highest Péclet numbers, these quasi-stationary solutions describe the shape of the area around the dendritic tip in the form of a smooth sphere in the isotropic case and a deformed sphere along the directions of anisotropy strength in the anisotropic case. A thermo-solutal selection criterion of the quasi-stationary growth mode of dendrites which includes arbitrary Péclet numbers is obtained. To demonstrate the selection of patterns, computational modelling of the quasi-stationary growth of crystals in a binary mixture is carried out.

The modelling makes it possible to obtain selected structures in the form of dendritic, fractal or planar crystals.

This article is part of the theme issue 'From atomistic interfaces to dendritic patterns'.

1. Introduction

The evolutionary behaviour of interfaces leading to developing multifarious pattern structures is of great significance in different phase transformation processes [1–5]. The Stefan-like moving boundary problems can be especially highlighted as very important tasks reflecting a complex dynamics of evolving patterns [6–12]. The phase interface in such problems is assumed to be atomically rough with thickness of the order of several interatomic distances. Not discussing this problem in detail (see works on phase-field modelling [13–26]) we shall neglect this atomic roughness and assume a sharp interface on the macroscopic length scale.

Methods of analytical and numerical description of the Stefan-type moving boundary problems can be classified as two problem-solving approaches: (i) to find the bulk temperature and solute concentration fields taking into account the phase interface conditions [9–11] and (ii) to formulate and solve the free-boundary problem for the phase interface function (deformation of the interfacial surface) [27–32]. The second approach can be directly used to evaluate the boundary integral suggested by Nash [27], discussed by Nash & Glicksman [28] and then independently detailed by Langer & Turski [29,30]. This method leans upon the Green function technique for the heat (and mass [33]) transfer equations, which allows a single integro-differential equation to be determined for the interface function. Note that Langer & Turski [29,30] developed their original theory to obtain the boundary integral for an Ising-like symmetric model when two phases contact each other at the interface. This theory has become the basis for stability and selection problems of dendritic interfaces [34–45]. Until quite recently, such a coupled thermo-diffusion problem with the help of boundary integral theory was studied only within the framework of the linear temperature gradient model by Kessler *et al.* [46]. Generalization to the complete coupling of the fields on the interface has been treated in [33].

The boundary integral method has a great impact on interface evolution and pattern formation in different free boundary problems (e.g. with the selection mode of stable dendritic growth [37–39]). This method can also be applied for modelling and testing several crystal growth theories or for comparison of the model results with the phase-field simulations. We demonstrate below how to use the boundary integral theory to also calculate interfacial shapes. Concluding this introductory section, let us especially emphasize that the present work generalizes the boundary integral theory for parabolic heat and mass transfer problems, extends it to the hyperbolic mass transfer in liquid, indicates how to simplify it in the case of steady-state interface propagation and demonstrates how to obtain the classical Ivantsov and Horvay–Cahn stationary solutions and growing shapes. Patterns selected in quasi-stationary solidification are modelled by the boundary integral and numerically solved by a specially developed iteration technique.

2. Thermo-chemical interface propagation under local equilibrium conditions (parabolic heat and mass transport)

Consider the solid/liquid interface propagation into an undercooled binary mixture caused by temperature and solutal gradients when the anisotropies of surface energy and growth kinetics play a preferable role in the evolutionary behaviour of the interface function (deformation of the interfacial surface). To obtain a time-dependent integro-differential equation for this function let us use the Green function technique previously developed by Nash & Glicksman [27,28] and Langer & Turski [29,30]. A solution procedure is divided into two simple steps which are concerned with a one-by-one consideration of purely thermal and thermo-chemical growth regimes.

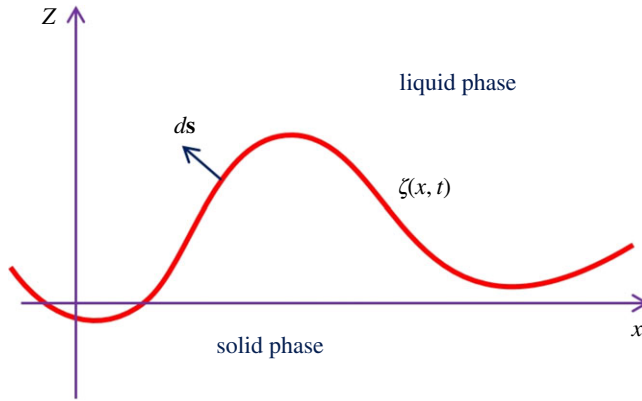


Figure 1. A curved solid/liquid interface.

(a) Thermally controlled interface propagation

First of all, we consider the thermally induced motion of the solid/liquid interface into an undercooled pure liquid. Let initially the solid/liquid interface be flat in the x -plane, which is perpendicular to the spatial direction z . The interface becomes curvilinear in the course of time due to the presence of instabilities and preferable local growth directions (figure 1). This curvilinear interface is designated by means of the interface function $z_{\text{interface}} = \zeta(x, t)$, where t is the phase transition time.

To find the interface function equation, two possible cases can be applied: (i) equal thermal diffusivities D_T in both phases [37,38] and (ii) a one-sided phase transition model where the transport flux is negligible from one of the phases at the moving interface [33]. Let us now consider the first of these approximations. The second one is used below when analysing the chemically controlled interface growth.

At the moving phase transition interface $\zeta(x, t)$, the Gibbs–Thomson and heat balance conditions hold true,

$$T = T_f - \frac{d_c Q}{c_p} K - \tilde{\beta} \left(V + \frac{\partial \zeta}{\partial t} \right) \quad (2.1)$$

and

$$D_T (\nabla T_s - \nabla T_l) \cdot ds = \frac{Q}{c_p} \left(V + \frac{\partial \zeta}{\partial t} \right) d^2x, \quad (2.2)$$

where $T(x, z, t)$ is the temperature, $\tilde{\beta}$ is the anisotropic coefficient describing the kinetic growth mode, T_f is the phase transition (freezing) temperature of the planar front at $\tilde{\beta} = 0$, d_c is the anisotropic capillary length, Q is the latent heat of phase transition released per unit volume of the solid, c_p is the specific heat, V is the constant growth velocity, ds is the vector element of the surface area pointing to the liquid phase, subscripts 's' and 'l' designate the solid and liquid phases, respectively, and the interface curvature K can be represented in the two- and three-dimensional cases in the form

$$K(\zeta) = -\frac{\partial^2 \zeta / \partial x^2}{[1 + (\partial \zeta / \partial x)^2]^{3/2}} \quad \text{and} \quad K(\zeta) = -\nabla \cdot \left[\frac{\nabla \zeta}{\sqrt{1 + (\nabla \zeta)^2}} \right]. \quad (2.3)$$

Introducing the coordinate system moving with velocity V , one can write down the heat transport equation in the liquid and solid phases as

$$\left(D_T \nabla^2 + V \frac{\partial}{\partial z} - \frac{\partial}{\partial t} \right) T = 0. \quad (2.4)$$

Green's function $G(p | p_1)$ corresponding to equation (2.4) satisfies the following equation:

$$\left(D_T \nabla_1^2 - V \frac{\partial}{\partial z_1} + \frac{\partial}{\partial t_1} \right) G(p | p_1) = -\delta(p - p_1), \quad (2.5)$$

where δ is the Dirac delta function, p is a short designation for the space-time point (x, z, t) , the operators on the left-hand side act on the subscripted variables x_1, z_1, t_1 and G vanishes for $t_1 > t$.

Multiplying equations (2.4) and (2.5) by G and T , respectively, with their further subtracting leads to

$$\begin{aligned} T(p) = D_T \int_{-\infty}^T dt_1 \int_{S_1} ds_1 [T(p_1) \nabla_1 G(p | p_1) - G(p | p_1) \nabla_1 T(p_1)] \\ + V \int_{-\infty}^T dt_1 \int_{A_1} d^2 x_1 dz_1 \frac{\partial}{\partial z_1} [G(p | p_1) T(p_1)], \end{aligned} \quad (2.6)$$

where A_1 is a region that includes the point p and excludes the interface, S_1 is the overall bounding surface of A_1 and ds_1 is the vector element of the area on S_1 pointing along the inward-directed normal to this surface.

Green's function determined by equation (2.5) can be expressed in terms of the corresponding Fourier transformation as

$$G(p | p_1) = \int \frac{d^j k}{(2\pi)^j} \int_C \frac{d\omega}{2\pi} \hat{G}(\mathbf{k}, \omega) e^{i\mathbf{k} \cdot (\mathbf{r} - \mathbf{r}_1) + i\omega(t - t_1)}, \quad (2.7)$$

where \mathbf{r} is the vector (x, z) , the contour C goes from $-\infty$ to $+\infty$ and passes over all singularities in the ω -plane in order to satisfy the causality condition [30], i is the imaginary unit, and parameter j equals 2 and 3 in the two- and three-dimensional cases, respectively. The integral kernel entering equation (2.7) can be represented as

$$\hat{G}(\mathbf{k}, \omega) = \frac{1}{D_T k^2 - iV k_z + i\omega}. \quad (2.8)$$

The inverse Fourier transform of equation (2.8) gives

$$\begin{aligned} G(p | p_1) = \frac{1}{(4\pi D_T \tau)^{j/2}} \exp \left(-\frac{\Sigma^2}{4D_T \tau} \right) \Bigg\} \\ \tau = t - t_1, \quad \Sigma^2 = |\mathbf{x} - \mathbf{x}_1|^2 + (z - z_1 + V\tau)^2. \end{aligned} \quad (2.9)$$

Because the temperature field is continuous at the phase transition interface, the contribution proportional to $\nabla_1 G$ in equation (2.6) cancels out. Now, we are able to calculate the second integral term containing $\nabla_1 T$ in equation (2.6) on the basis of expression (2.2). Keeping in mind that the last term in equation (2.6) is equal to T_∞ [30], we get

$$T(p) = T_\infty + \frac{Q}{c_p} \int_{-\infty}^T dt_1 \int_{-\infty}^{\infty} \int_{-\infty}^{\infty} d^2 x_1 G(p | p_1) \left(V + \frac{\partial \zeta_1}{\partial t_1} \right). \quad (2.10)$$

Here, T_∞ stands for the temperature far from the solid/liquid interface and ζ_1 designates $\zeta(\mathbf{x}_1, t_1)$.

If we now move the point p closer to the phase interface and take into account equations (2.1) and (2.10), we come to

$$\Delta - d_c K - \beta \left(V + \frac{\partial \zeta}{\partial t} \right) - \int_{-\infty}^T dt_1 \int_{-\infty}^{\infty} \int_{-\infty}^{\infty} d^2 x_1 \bar{G}(p | p_1) \left(V + \frac{\partial \zeta(\mathbf{x}_1, t_1)}{\partial t_1} \right) = 0, \quad (2.11)$$

where $\Delta = (T_f - T_\infty)c_p/Q$ is the dimensionless undercooling and $\beta = \tilde{\beta}c_p/Q$ is the kinetic coefficient, and

$$\bar{G}(p | p_1) = \frac{1}{(4\pi D_T \tau)^{j/2}} \exp \left(-\frac{\bar{\Sigma}^2}{4D_T \tau} \right), \quad \bar{\Sigma}^2 = |\mathbf{x} - \mathbf{x}_1|^2 + [\zeta(\mathbf{x}, t) - \zeta(\mathbf{x}_1, t_1) + V\tau]^2.$$

Let us introduce the following dimensionless variables (ρ is a characteristic length scale):

$$x' = \frac{x}{\rho}, \quad x'_1 = \frac{x_1}{\rho}, \quad \tau' = \frac{V\tau}{\rho}, \quad \zeta' = \frac{\zeta}{\rho}, \quad t' = \frac{Vt}{\rho}, \quad t'_1 = \frac{Vt_1}{\rho} \quad \text{and} \quad \tau' = t' - t'_1. \quad (2.12)$$

Substituting (2.12) into the integral equation (2.11) and omitting primes for simplicity, we arrive at

$$\Delta - \frac{dc}{\rho}K - \beta V \left(1 + \frac{\partial \zeta(\mathbf{x}, t)}{\partial t} \right) = I_{\zeta}^T, \quad (2.13)$$

where

$$I_{\zeta}^T = P_T \int_0^{\infty} \frac{d\tau}{2\pi\tau} \int_{-\infty}^{\infty} dx_1 \left[1 + \frac{\partial \zeta(x_1, t - \tau)}{\partial t} \right] \times \exp \left\{ -\frac{P_T}{2\tau} [(x - x_1)^2 + (\zeta(x, t) - \zeta(x_1, t - \tau) + \tau)^2] \right\} \quad (2.14)$$

in the two-dimensional case and

$$I_{\zeta}^T = P_T^{3/2} \int_0^{\infty} \frac{d\tau}{(2\pi\tau)^{3/2}} \int_{-\infty}^{\infty} \int_{-\infty}^{\infty} d^2x_1 \left[1 + \frac{\partial \zeta(\mathbf{x}_1, t - \tau)}{\partial t} \right] \times \exp \left\{ -\frac{P_T}{2\tau} [|\mathbf{x} - \mathbf{x}_1|^2 + (\zeta(\mathbf{x}, t) - \zeta(\mathbf{x}_1, t - \tau) + \tau)^2] \right\} \quad (2.15)$$

in the three-dimensional case. Here, $P_T = \rho V / (2D_T)$ is the thermal Péclet number, and $K(\zeta(\mathbf{x}, t))$ is defined by expressions (2.3). Equation (2.13) represents the dimensionless integro-differential equation for the interface function in two and three spatial dimensions if the phase transition is thermally controlled.

An important point is that expressions (2.13) and (2.14) represent the basis for the previously developed stability and selection theories of dendritic growth [39–43] in the case of two-dimensional geometry. In addition, equations (2.13) and (2.15) transform to the corresponding expressions of [2,37] in the limiting case $\partial \zeta / \partial t = 0$, and in the absence of growth anisotropy $\tilde{\beta} = 0$ if we are dealing with the three-dimensional case. Note that equations (2.13)–(2.15) have been used by Barbieri & Langer [38] in the absence of interface atomic kinetics, $\tilde{\beta} = 0$ in two- and three-dimensional growth geometries.

(b) Thermally and chemically controlled interface propagation

In this section, we consider the so-called thermo-chemical interface propagation occurring as a result of temperature and solutal gradients when the anisotropies of surface energy and growth kinetics dictate the preferable growth direction. Such a dynamic scenario of interface propagation occurs in a binary mixture during the intermediate stage of phase transformation between the diffusion-limited and pure thermally controlled regimes [47,48].

An isobaric binary system consisting of non-interacting A - and B -kinds of particles (solvent and solute) is under study when the phase transition occurs without the mass density change (i.e. without shrinkage of phases). We also neglect any convective processes of either heat or solute (A - and B -particles) and, as above, consider the conductive mechanism of heat (and mass) transfer. Keeping in mind that the chemical diffusion in the solid phase is much slower than that in the liquid phase [9,49–53], we consider the diffusion of B -particles in liquid only (one-sided model). Therefore, the mass balance equation, written out in addition to the heat balance equation (2.2), takes the form

$$-D_C \nabla C_l \cdot d\mathbf{s} = (1 - k_0)C_l \left(V + \frac{\partial \zeta}{\partial t} \right) d^2x, \quad (2.16)$$

where D_C is the chemical diffusivity of the solute (B -particles), k_0 is the equilibrium partition coefficient, C_l is the solute concentration of the binary mixture in the liquid phase and C_i is the

interfacial concentration. The Gibbs–Thomson condition (2.1) for thermo-chemical growth has the form

$$T = T_f - \frac{d_c Q}{c_p} K + m C_i - \tilde{\beta} \left(V + \frac{\partial \zeta}{\partial t} \right), \quad (2.17)$$

where m designates the liquidus slope. The mass transport equation in the moving frame of reference is governed by

$$\left(D_C \nabla^2 + V \frac{\partial}{\partial z} - \frac{\partial}{\partial t} \right) C_1 = 0. \quad (2.18)$$

It is important to note that the interface kinetics previously introduced in the thermal and thermo-chemical problem of solidification has been validated independently by means of other alternative approaches [54,55]. This makes possible a flexible description of thermal and chemical processes at different stages of dendrite growth [56].

Equations (2.4) and (2.18) are equivalent and coincide after replacing D_T by D_C . Therefore, by analogy with the solution (2.6) for temperature, the solution for the mass transport equation is described by

$$\begin{aligned} C_1(p) = D_C \int_{-\infty}^T dt_1 \int_{S_1} d\mathbf{s}_1 \{ \nabla_1 [C_1(p_1) G_C(p | p_1)] - 2 G_C(p | p_1) \nabla_1 C_1(p_1) \} \\ + V \int_{-\infty}^T dt_1 \int_{\Lambda_1} d^2 x_1 dz_1 \frac{\partial}{\partial z_1} [G_C(p | p_1) C_1(p_1)]. \end{aligned} \quad (2.19)$$

Here, the integral of $\nabla_1 [C_1(p_1) G_C(p | p_1)]$ becomes zero in accordance with the Kelvin–Stokes theorem of integration of the nabla operator about a closed path S_1 . Next, one can easily find the integral corresponding to the contribution $G_C(p | p_1) \nabla_1 C_1(p_1)$ by means of the boundary condition (2.16) if neglecting the concentration flux in the solid phase. The last contribution in (2.19) equals the solute concentration $C_{1\infty}$ in liquid far from the solid/liquid interface (for details, see [30]). As a result, we are able to rewrite expression (2.19) as

$$\left. \begin{aligned} C_1(p) &= C_{1\infty} + 2(1 - k_0) \int_{-\infty}^T dt_1 \int_{-\infty}^{\infty} \int_{-\infty}^{\infty} d^2 x_1 G_C(p | p_1) C_i(\mathbf{x}_1, t_1) \left(V + \frac{\partial \zeta_1}{\partial t_1} \right), \\ G_C(p | p_1) &= \frac{1}{2(4\pi D_C \tau)^{j/2}} \exp \left(-\frac{\Sigma^2}{4D_C \tau} \right). \end{aligned} \right\} \quad (2.20)$$

Combining expressions (2.13) and (2.17), one can obtain the interfacial concentration

$$C_i(\mathbf{x}, t) = -\frac{Q}{mc_p} \left[\Delta - \frac{d_c}{\rho} K - \beta V \left(1 + \frac{\partial \zeta(\mathbf{x}, t)}{\partial t} \right) - I_\zeta^T \right]. \quad (2.21)$$

Now the interface function $\zeta(\mathbf{x}, t)$ is determined from expressions (2.20) and (2.21) and satisfies the following time-dependent integro-differential equation:

$$-\frac{Q}{mc_p} \left[\Delta - \frac{d_c}{\rho} K - \beta V \left(1 + \frac{\partial \zeta(\mathbf{x}, t)}{\partial t} \right) - I_\zeta^T \right] - C_{1\infty} = I_\zeta^C, \quad (2.22)$$

where

$$\begin{aligned} I_\zeta^C &= (1 - k_0) P_C \int_0^\infty \frac{d\tau}{2\pi\tau} \int_{-\infty}^\infty dx_1 C_i(x_1, t - \tau) \left[1 + \frac{\partial \zeta(x_1, t - \tau)}{\partial t} \right] \\ &\times \exp \left\{ -\frac{P_C}{2\tau} [(x - x_1)^2 + (\zeta(x, t) - \zeta(x_1, t - \tau) + \tau)^2] \right\} \end{aligned} \quad (2.23)$$

in the two-dimensional geometry and

$$\begin{aligned} I_\zeta^C &= (1 - k_0) P_C^{3/2} \int_0^\infty \frac{d\tau}{(2\pi\tau)^{3/2}} \int_{-\infty}^\infty \int_{-\infty}^\infty d^2 x_1 C_i(\mathbf{x}_1, t - \tau) \left[1 + \frac{\partial \zeta(x_1, t - \tau)}{\partial t} \right] \\ &\times \exp \left\{ -\frac{P_C}{2\tau} [|\mathbf{x} - \mathbf{x}_1|^2 + (\zeta(\mathbf{x}, t) - \zeta(\mathbf{x}_1, t - \tau) + \tau)^2] \right\} \end{aligned} \quad (2.24)$$

in the three-dimensional geometry. Here, $P_C = \rho V / (2D_C) = P_T D_T / D_C$ stands for the chemical Péclet number. Note that P_C in equations (2.23) and (2.24) are pulled out of the integrals because they include only constant values of V and ρ related to the quasi-stationary growth mode.

In consideration of the presently formulated thermo-chemical boundary integral, we have used a simple model of a dilute binary mixture. A more realistic boundary integral model of multi-component non-isothermal mixtures can be developed if the diffusion fluxes are written via chemical potentials and, respectively, thermodynamic potentials from all elemental and energetic contributions of the whole mixture, as has been done in models based on the phase-field method [57,58].

Concluding this section, let us underline that the boundary integral that describes the curvilinear interface function $\zeta(\mathbf{x}, t)$ for the thermo-chemical Stefan problem is given by equation (2.22), whose thermal and concentration contributions are determined by expressions (2.14), (2.15), (2.23) and (2.24). As a special note, the isothermal solute diffusion-limited solidification is defined by equation (2.22). Namely, setting $D_T \rightarrow \infty$ and $P_T \rightarrow 0$ (in this limiting case, I_ζ^T determined by equations (2.14) and (2.15) vanishes), this case is also described.

3. Thermo-chemical interface propagation under local non-equilibrium conditions (parabolic heat and hyperbolic mass transport)

The aforementioned thermo-chemical boundary integral theory can only be applied for the description of local equilibrium phase transition. Modern experimental facilities allow us to obtain large undercoolings and cooling rates leading to substantial temperature and concentration gradients as well as high rates of phase interface propagation. For instance, the electromagnetic levitation technique allows the liquid phase to be undercooled by up to 400 K below its liquidus temperature. This leads to the highest solidification velocities ranging from 10 to 100 m s⁻¹ [59]. A theoretical description of such deeply undercooled phase transitions depends upon the hyperbolic mass transport equation for solute diffusion [47]. Such a hyperbolic approach has been validated by comparison with experimental data [60], by atomistic simulations of the solute trapping effect for fast fronts [61] and by coarse-graining derivations of the phase-field equations [62].

(a) Mathematical background of the hyperbolic mass transport

Taking the aforesaid into account, we consider the phase interface $\zeta(\mathbf{x}, t)$ propagating into a metastable medium under local non-equilibrium conditions which are described by the hyperbolic-type mass transfer equation [47] in the laboratory coordinate system

$$\left(D_C \nabla^2 - \frac{\partial}{\partial t} - \tau_D \frac{\partial^2}{\partial t^2} \right) C_1 = 0, \quad (3.1)$$

where τ_D stands for the local diffusion relaxation time of mass flux to its steady-state value. As the temperature field relaxes to its local equilibrium much faster, we use, as before, the parabolic temperature conductivity equation (2.4).

At the curved solid/liquid front $\zeta(\mathbf{x}, t)$, the mass conservation has the form

$$-D_C \nabla C_1 \, ds = (1 - k_v) C_i \left(V + \frac{\partial \zeta}{\partial t} \right) d^2 x + \tau_D \frac{\partial}{\partial t} \left[(1 - k_v) C_i \left(V + \frac{\partial \zeta}{\partial t} \right) \right] d^2 x, \quad (3.2)$$

where the velocity-dependent chemical segregation coefficient is [63]

$$k_v = \begin{cases} \frac{(1 - v^2/V_D^2)k_0 + v/V_{DI}}{(1 - v^2/V_D^2)[1 - (1 - k_0)C_i] + v/V_{DI}}, & v < V_D, \\ 1, & v \geq V_D, \end{cases} \quad (3.3)$$

where $v = V + \partial\zeta/\partial t$, and V_D and V_{DI} are the bulk and interface diffusion speeds, respectively. Note that the thermal fluxes at the phase interface, as before, are connected by means of the boundary condition (2.2).

The Gibbs–Thomson condition now becomes

$$T = T_f - d_c T_Q K + m_v C_i - \tilde{\beta} \left(V + \frac{\partial\zeta}{\partial t} \right), \quad (3.4)$$

where $m_v = dT/dC_i$ is the change of temperature at the interface with respect to the change of concentration as a function of the interface velocity at constant pressure and $T_Q = Q/c_p$. The velocity-dependent liquidus slope m_v takes the form [64]

$$m_v(v) = \begin{cases} \frac{m}{k_0 - 1} \left(1 - k_v + \ln \left(\frac{k_v}{k_0} \right) + \frac{(1 - k_v)^2 v}{V_D} \right), & v < V_D, \\ \frac{-m \ln k_0}{k_0 - 1}, & v \geq V_D. \end{cases} \quad (3.5)$$

(b) Boundary integral equations

The Green function G_{CH} for the hyperbolic mass transport equation (3.1) satisfies

$$\left(D_C \nabla_1^2 + \frac{\partial}{\partial t_1} - \tau_D \frac{\partial^2}{\partial t_1^2} \right) G_{CH}(p | p_1) = -\delta(p - p_1), \quad (3.6)$$

where subscript CH designates the hyperbolic solution for concentration. For two and three dimensions, G_{CH} has been determined by Morse & Feshbach [65] as

$$G_{CH}(p | p_1) = \begin{cases} \frac{VG_2(p | p_1)}{2\pi D_C \rho}, & \text{two-dimensional case,} \\ \frac{VG_3(p | p_1)}{8\pi \rho \sqrt{\tau_D} D_C^{3/2}}, & \text{three-dimensional case,} \end{cases} \quad (3.7)$$

where

$$G_2 = \begin{cases} \exp \left(-\frac{\tau}{\tau_*} \right) \cosh \left(\tau_*^{-1} \sqrt{\tau^2 - R_{2D}^2} \right) \frac{\theta(\rho(\tau - R_{2D})/W)}{\sqrt{\tau^2 - R_{2D}^2}}, & \text{with } R_{2D} < \tau, \\ 0, & \text{with } R_{2D} \geq \tau \end{cases} \quad (3.8)$$

and

$$G_3 = \begin{cases} \frac{v\delta(\rho(\tau - R_{3D})/W)}{R_{3D} \exp[\tau/\tau_*]} + \frac{J_1 \left(\tau_*^{-1} \sqrt{R_{3D}^2 - \tau^2} \right) \theta(\rho(\tau - R_{3D})/W)}{\sqrt{R_{3D}^2 - \tau^2} \exp[\tau/\tau_*]}, & \text{with } R_{3D} < \tau, \\ 0, & \text{with } R_{3D} \geq \tau, \end{cases} \quad (3.9)$$

where $R_{jD}^2 = P_C \tau_* [|\mathbf{x} - \mathbf{x}_1|^2 + (z - z_1 + \tau)^2]$, $j = 2$ and $j = 3$ in the two- and three-dimensional cases, respectively, ρ is a characteristic length scale, J_1 is the Bessel function of the first kind, θ is the Heaviside step function, $\tau_* = 2\tau_D V/\rho$, $V_D = \sqrt{D_C/\tau_D}$, $\tau = t - t_1$, $W = V/V_D$, $v = 2D_C/V_D$, $P_C = \rho V/(2D_C) = W^2/\tau_*$ is the solutal Peclet number, and all length and time scales, as before, are measured in units of ρ and ρ/V , respectively. Note that Green's functions (3.8) and (3.9) turn to zero at $\tau < R_{2D}$ and $\tau < R_{3D}$, respectively. An important point is that solution (3.7) transforms to the corresponding parabolic Green's functions determined in the preceding section in the limiting case $\tau_* \rightarrow 0$ (see also [27,33]).

We especially note that Morse & Feshbach [65] have not considered transport velocities reaching and exceeding the characteristic speeds for the propagation of disturbances, i.e. they have written the Green functions (3.8) and (3.9) only for the case of velocities $W = V/V_D < 1$. In the case of alloys, the solidification front can reach or even exceed the atomic diffusion speed.

Therefore, we have included in equations (3.8) and (3.9) the conditions $R_{jD} < \tau$ and $R_{jD} \geq \tau$, which are equivalent to regimes with the growth velocity smaller than the maximum diffusion speed, $W < 1$; $V < V_D$, and regimes with the growth velocity larger than the maximum diffusion speed, $W \geq 1$; $V \geq V_D$, respectively.

Now, the interfacial concentration at $z = \zeta$ should be written as

$$C_i(\mathbf{x}, t) = C_{l\infty} + I_\zeta^{\text{CH}}, \quad (3.10)$$

$$I_\zeta^{\text{CH}} = \begin{cases} \frac{P_C}{\pi} \int_0^\infty d\tau \int_{-\infty}^\infty dx_1 F(x_1, t - \tau) G_2(p | p_1), & \text{two-dimensional case,} \\ \frac{P_C^{3/2}}{2\pi\sqrt{\tau_*}} \int_0^\infty d\tau \int_{-\infty}^\infty \int_{-\infty}^\infty d^2x_1 F(\mathbf{x}_1, t - \tau) G_3(p | p_1), & \text{three-dimensional case} \end{cases} \quad (3.11)$$

and

$$\left. \begin{aligned} F(\mathbf{x}_1, t - \tau) &= (1 - k_v)(1 + \dot{\zeta}(\mathbf{x}_1, t - \tau))C_i(\mathbf{x}_1, t - \tau) \\ &\quad - \frac{\tau_*}{2} \frac{\partial}{\partial \tau} [(1 - k_v)(1 + \dot{\zeta}(\mathbf{x}_1, t - \tau))C_i(\mathbf{x}_1, t - \tau)], \quad \text{with } V < V_D, \\ F(\mathbf{x}_1, t - \tau) &= 0, \quad \text{with } V \geq V_D, \end{aligned} \right\} \quad (3.12)$$

where $\dot{\zeta} = \partial\zeta/\partial t$, k_v is calculated at the time moment $t - \tau$ and \mathbf{x}_1 must be replaced by x_1 in the two-dimensional case. Note that P_C in equation (3.11) are pulled out of the integrals because they include only constant values of V and ρ related to the quasi-stationary growth mode. Two inequalities in equation (3.12) follow from equations (3.8) and (3.9) as well as from the conditions of the diffusionless solidification $C_i = 0$ and $k_v = 1$ with $V \geq V_D$ ($W \geq 1$; see equation (3.3)).

A unified integro-differential equation for the interface function $\zeta(\mathbf{x}, t)$ is determined from the Gibbs–Thomson condition (2.17) or (2.22) with allowance for the hyperbolic solutions (3.10)–(3.12) as

$$-\frac{Q}{m_v c_p} \left[\Delta - \frac{d_c}{\rho} K - \beta V \left(1 + \frac{\partial \zeta(\mathbf{x}, t)}{\partial t} \right) - I_\zeta^T \right] - C_{l\infty} = I_\zeta^{\text{CH}}. \quad (3.13)$$

This equation describes the interface evolution for the thermo-chemical Stefan model when the thermal field is defined by the solution of the differential equation of the parabolic type and the solute field is described by the differential equation of the hyperbolic type. As follows from equations (3.10)–(3.12), the complete equation (3.13) is true for $V < V_D$. If $V \geq V_D$, one obtains $I_\zeta^{\text{CH}} = 0$. As a limiting case, equation (3.13) transforms to equation (2.22) for the parabolic thermo-chemical model when $V \ll V_D$, $W \ll 1$.

4. Steady-state interface propagation

The boundary integrals derived in the preceding sections can be simplified in the practically important solidification process with a constant velocity V , $\partial\zeta/\partial t = 0$. This section is concerned with modifications of the thermal and concentration integrals for parabolic and hyperbolic transport.

(a) Thermo-solutal parabolic problem

The right-hand side of equation (2.14) can be evaluated over τ for two dimensions, $\zeta = \zeta(x)$, by taking into account that the modified Bessel function of zero order is expressed as [66]

$$K_0(z) = \int_0^\infty \exp(-z \cosh u) du.$$

Then, equations (2.13) and (2.14) have the form of a single modified boundary integral,

$$\Delta - \frac{d_c}{\rho} K - \beta V = I_\zeta^T = \frac{P_T}{\pi} \int_{-\infty}^{\infty} dx_1 \exp\{-P_T[\zeta(x) - \zeta(x_1)]\} \\ \times K_0 \left(P_T \sqrt{(x - x_1)^2 + [\zeta(x) - \zeta(x_1)]^2} \right), \quad (4.1)$$

which determines the curved interface function $\zeta(x)$ for the two-dimensional thermal problem.

Keeping in mind that the modified Bessel function of $\frac{1}{2}$ -order [66] reads as

$$K_{1/2}(z) = \frac{\pi}{2} [I_{-1/2}(z) - I_{1/2}(z)], \\ I_{\pm 1/2} = \frac{1}{\pi} \int_0^\pi \exp(z \cos \theta) \cos \frac{\theta}{2} d\theta \mp \frac{1}{\pi} \int_0^\infty \exp(-z \cosh u \mp \frac{u}{2}) du,$$

integrating the right-hand side of expression (2.15) over τ and substituting the result into equation (2.13), one can obtain the steady-state boundary integral in the three-dimensional case, $\zeta = \zeta(x, y)$, as

$$\Delta - \frac{d_c}{\rho} K - \beta V = I_\zeta^T \equiv 2 \left(\frac{P_T}{2\pi} \right)^{3/2} \int_{-\infty}^{\infty} \int_{-\infty}^{\infty} dx_1 dy_1 \exp\{-P_T[\zeta(x, y) - \zeta(x_1, y_1)]\} \frac{K_{1/2}(P_T \sqrt{b_P})}{b_P^{1/4}}, \\ b_P = (x - x_1)^2 + (y - y_1)^2 + [\zeta(x, y) - \zeta(x_1, y_1)]^2. \quad (4.2)$$

This integral characterizes the interface function $\zeta(x, y)$ for the thermal problem in three dimensions. Note that equations (4.1) and (4.2) have been previously used by Pelcé [2] and Kessler *et al.* [46] in their analyses of stable dendritic growth.

In the case of the coupled thermo-solutal problem, keeping in mind equations (2.21) and (2.22), we have the following equation for the interface function, which includes the thermal and concentration contributions I_ζ^T and I_ζ^C :

$$-\frac{Q}{mc_p} \left(\Delta - \frac{d_c}{\rho} K - \beta V - I_\zeta^T \right) - C_{1\infty} = I_\zeta^C. \quad (4.3)$$

Here, I_ζ^T is determined by equations (4.1) and (4.2) in the two- and three-dimensional case, respectively.

Taking into account a certain analogy between the thermal and concentration problems, we are now able to find the concentration integrals I_ζ^C as

$$I_\zeta^C = (1 - k_0) \frac{P_C}{\pi} \int_{-\infty}^{\infty} dx_1 C_i(x_1) \exp\{-P_C[\zeta(x) - \zeta(x_1)]\} K_0 \left(P_C \sqrt{(x - x_1)^2 + [\zeta(x) - \zeta(x_1)]^2} \right) \quad (4.4)$$

in the two-dimensional space and

$$I_\zeta^C = 2(1 - k_0) \left(\frac{P_C}{2\pi} \right)^{3/2} \int_{-\infty}^{\infty} \int_{-\infty}^{\infty} dx_1 dy_1 C_i(x_1, y_1) \\ \times \exp\{-P_C[\zeta(x, y) - \zeta(x_1, y_1)]\} \frac{K_{1/2}(P_C \sqrt{b_P})}{b_P^{1/4}} \quad (4.5)$$

in the three-dimensional space.

Concluding this subsection, let us especially underline that equation (4.3) determines the steady-state interface function $\zeta(x, y)$ for the thermo-solutal parabolic Stefan problem, and the integrals I_ζ^T and I_ζ^C are determined by expressions (4.1), (4.2) and (4.4), (4.5).

(b) Thermo-solutal problem in the case of hyperbolic mass transfer

Let us now integrate expressions (3.11) for the quasi-stationary solidification. Completing the squares in the arguments of the hyperbolic cosine and Bessel function J_1 in expressions (3.8) and

(3.9) and integrating over τ , we arrive at the modified concentration integrals in the two- and three-dimensional geometries, respectively [67]:

$$I_{\zeta}^{\text{CH}} = \frac{P_C(1 - k_v(V))}{\pi\sqrt{1 - P_C\tau_*}} \int_{-\infty}^{\infty} K_0 \left(\frac{P_C\sqrt{b_H}}{1 - P_C\tau_*} \right) \exp \left(-\frac{P_C(\zeta(x) - \zeta(x_1))}{1 - P_C\tau_*} \right) C_i(x_1) dx_1 \quad (4.6)$$

and

$$I_{\zeta}^{\text{CH}} = \frac{2(1 - k_v(V))}{\sqrt{1 - P_C\tau_*}} \left(\frac{P_C}{2\pi} \right)^{3/2} \int_{-\infty}^{\infty} \int_{-\infty}^{\infty} K_{1/2} \left(\frac{P_C\sqrt{b_H}}{1 - P_C\tau_*} \right) \times \exp \left(-\frac{P_C(\zeta(\mathbf{x}) - \zeta(\mathbf{x}_1))}{1 - P_C\tau_*} \right) \frac{C_i(\mathbf{x}_1)}{b_H^{1/4}} d^2x_1. \quad (4.7)$$

Here, K_0 and $K_{1/2}$ represent the modified Bessel functions, and $b_H = (1 - P_C\tau_*)|\mathbf{x} - \mathbf{x}_1|^2 + (\zeta(\mathbf{x}) - \zeta(\mathbf{x}_1))^2$.

Expressions (4.6) and (4.7) are true for $V < V_D$ (as in the non-steady case described by equations (3.10)–(3.12)). If $V \geq V_D$, one obtains $I_{\zeta}^{\text{CH}} = 0$ in equations (4.6) and (4.7). This result has a clear physical meaning [68]: when the interface velocity V is equal to or greater than the diffusive speed V_D , a profile of concentration cannot be created ahead of the interface and the system solidifies by the diffusionless mechanism. Note that the transition to diffusionless solidification proceeds sharply with an abrupt drop point at $V = V_D$ in the kinetic curves ‘dendrite velocity–undercooling’ [47].

The steady-state parabolic heat transfer therewith is described by integrals I_{ζ}^{T} from expressions (4.1) and (4.2), whereas the interface function $\zeta(x, y)$ follows from equation (3.13) at $\partial\zeta/\partial t = 0$. As a result, the equation for ζ is described by

$$-\frac{Q}{m_v c_p} \left[\Delta - \frac{d_c}{\rho} K - \beta V - I_{\zeta}^{\text{T}} \right] - C_{1\infty} = I_{\zeta}^{\text{CH}}. \quad (4.8)$$

(c) Selection criterion of stable dendritic growth

This subsection is concerned with a selection criterion $\sigma^* = 2d_0 D_T / (\rho^2 V)$ that determines a combination between the dendrite tip diameter ρ and its tip velocity V . We obtain this combination on the basis of dendritic growth theory developed in a similar paper in the present theme issue [20]. The criterion for σ^* given below generalizes previously known criteria and comprises the hyperbolic mass transfer mechanism in a binary melt, growth kinetics and forced convection. The main idea of how to derive this criterion consists in developing the laws for formal transition between the hyperbolic and parabolic equations that describe the solute concentration in the liquid phase.

Let us initially emphasize an important feature of hyperbolic integrals (4.6) and (4.7) characterizing the steady-state dendritic growth at high solidification velocities V (at high growth Péclet numbers P_T). This feature resides in the fact that the integrals (4.6) and (4.7) (for the transport described by the hyperbolic equation) transform into equations (4.4) and (4.5) (which are true for the transport described by the parabolic equation) after introducing new spatial coordinates (subscript ‘new’) of the form

$$x_1 = \sqrt{1 - W^2} x_{1\text{new}}, \quad x = \sqrt{1 - W^2} x_{\text{new}} = \rho\sqrt{\xi}\eta, \quad z = \sqrt{1 - W^2} z_{\text{new}} = \frac{\rho}{2}(\eta - \xi) \quad (4.9)$$

(and $y_1 = \sqrt{1 - W^2} y_{1\text{new}}$, $y = \sqrt{1 - W^2} y_{\text{new}}$ in the three-dimensional geometry). Indeed, keeping in mind that $\zeta(x) - \zeta(x_1) = (x_1^2 - x^2)/2$ (and $\zeta(\mathbf{x}) - \zeta(\mathbf{x}_1) = (x_1^2 - x^2)/2 + (y_1^2 - y^2)/2$ in the three-dimensional case), and $k_v = k_v$ becomes k_0 , one can conclude that expressions (4.6) and (4.7) become identical to expressions (4.4) and (4.5). Expressions (4.9), in turn, imply that the hyperbolic problem transforms into the parabolic one after substitution $\rho/\sqrt{1 - W^2} = \rho/(1 - P_C\tau_*)$ by ρ_{new} in coordinates x_{new} , y_{new} and z_{new} . It is important to highlight here that the selection parameter σ^* (or combination $\rho^2 V$) remains constant during dendritic growth. By this we mean that the tip

velocity $(1 - W^2)V$ should be replaced by V_{new} ($\rho_{\text{new}}^2 V_{\text{new}} = \text{const.}$), while the chemical Péclet number $P_C = \rho V / (2D_C)$ becomes $P_C^* \equiv \rho_{\text{new}} V_{\text{new}} / (2D_C \sqrt{1 - W^2})$.

Expression (3.25) of [20] determines the selection criterion for the parabolic mass transfer mechanism. Taking the aforementioned remarks into account, we rewrite this criterion for the hyperbolic mass transfer mechanism and n -fold symmetry of crystal growth as (for the sake of simplicity, we omit subscript ‘new’ and designate through V and ρ the dendrite tip velocity and its tip diameter for the hyperbolic problem)

$$\sigma^* = \frac{2d_0 D_T}{\rho^2 V} = \frac{\sigma_0 \alpha_d^{7/n} A_n^{7/n}}{1 + b \bar{\tau}_n^{v_n}} \left\{ \frac{1}{[1 + a_1 \alpha_d^{2/n} A_n^{2/n} P_T (1 + \delta_0 D_T \beta_0 / d_0)]^2} + \frac{2m_v C_i (k_v - 1) D_T}{[1 + a_2 \alpha_d^{2/n} A_n^{2/n} P_C^* (1 + \delta_0 D_C \beta_0 / d_0 D_C)]^2 T_Q D_C} \right\}, \quad W < 1 \quad (4.10)$$

and

$$\sigma^* = \frac{2d_0 D_T}{\rho^2 V} = \frac{\sigma_0 \alpha_d^{7/n} A_n^{7/n}}{1 + b \bar{\tau}_n^{v_n}} \cdot \frac{1}{[1 + a_1 \alpha_d^{2/n} A_n^{2/n} P_T (1 + \delta_0 D_T \beta_0 / d_0)]^2}, \quad W \geq 1,$$

where d_0 is the capillary constant, U is the velocity of forced flow, α_d is the surface energy anisotropy, β_0 is the kinetic constant, and σ_0, b, a_1, a_2 and δ_0 are constants.

Here, $k_v = k_v(V)$, $m_v = m_v(V)$ and C_i are determined by relations (3.3), (3.5) and (3.10), respectively. Let us note that, in criterion (4.10), we have rescaled only the chemical Péclet number (the growth Péclet number P_g remains unchanged). This is due to the fact that the rescaling procedure is concerned only with the chemical dendrite selection criterion (the second term in curly brackets of (4.10)) induced by changing the mass transfer from parabolic to hyperbolic. The selection parameter (4.10) has only the thermal contribution in the rapid solidification limit $W \geq 1$ ($V \geq V_D$) when the concentration distribution in liquid is frozen and does not contain any inhomogeneities. The hydrodynamic contribution entering in $\bar{\tau}_n$ completely coincides with the parabolic growth problem because this contribution plays a key role only in the limit of slow velocity V when the hyperbolic mass transfer does not occur and the crystal growth proceeds in accordance with the parabolic heat and mass transfers.

The criterion (4.10) contains previously found parabolic selection criteria discussed in [20,69]. The criterion describes the thermally and solutally limited regimes under the control of the anisotropy of surface energy. Limiting cases of the solely kinetic regime of dendritic growth, an influence of kinetic anisotropy and the transition from the thermo-solutally controlled to the kinetically limited regime are given in [43,56]. In these works, asymptotic solutions and sewing with the kinetic regime are shown and discussed. Using asymptotics for the kinetic regime, one can obtain the selection criterion, which includes the kinetic anisotropy additionally to equation (4.10).

In summary, the criterion (4.10) extends the growth criteria derived for the transport described by the parabolic equation and includes hyperbolic mass transfer playing a substantial role in the case of rapid dendritic growth processes [47]. This criterion also generalizes the described limiting regimes and gives a stable relation between V and ρ for the n -fold crystal growth symmetry with allowance for the kinetics and surface energy anisotropies and a forced convective flow.

5. Steady-state Ivantsov solutions

This section is concerned with the question of how to derive the steady-state solutions describing the growth of a parabolic platelet (two-dimensional growth) and a paraboloid of revolution (three-dimensional growth) in the case of parabolic and hyperbolic transfer. At the first instance, we turn our attention to the classical Ivantsov solutions for the thermo-chemical problem.

(a) Ivantsov solutions

Let us demonstrate that the boundary integrals (2.13)–(2.15) and (2.22)–(2.24) include the classical Ivantsov solutions [70,71], which describe the steady-state propagation of a parabolic platelet and

a paraboloid of revolution. We assume that the surface energy and kinetic effects are negligible ($d_c = 0$, $\beta = 0$) and $\partial\zeta/\partial t = 0$.

Let us begin with the thermally controlled growth of a parabolic platelet and consider expressions (2.13) and (2.14). Initially, we substitute the parabolic shape $\zeta(x) = -x^2/2$ and replace the integration variable τ by ω as

$$\omega = \frac{(x - x_1)^2}{2\tau}.$$

Then we integrate the right-hand side of expression (2.14) over x_1 and conclude that the resultant expression is independent of x . Combining the obtained expression and equation (2.13), we come to the liquid undercooling Δ , which coincides with the thermal Ivantsov solution [33,40,46,70,71]

$$\begin{aligned} I_\zeta^T = \Delta &= \sqrt{\frac{P_T}{\pi}} \int_0^\infty \frac{\exp(-P_T\omega)}{\sqrt{\omega}(1+\omega)} d\omega \\ &= \sqrt{\pi P_T} \exp(P_T) \operatorname{erfc}(\sqrt{P_T}) = P_T \exp(P_T) \int_1^\infty \frac{\exp(-P_T\eta)}{\sqrt{\eta}} d\eta. \end{aligned} \quad (5.1)$$

Here, we use the following integral expression [67]:

$$\int_1^\infty \frac{\exp(-P_T u)}{u\sqrt{u-1}} du = \pi \operatorname{erfc}(\sqrt{P_T}).$$

When we are dealing with the three-dimensional motion of a paraboloid of revolution $\zeta(x, y) = -x^2/2 - y^2/2$, we replace two variables τ and y_1 by ω and z_1 , respectively, in equation (2.15) as

$$\omega = \frac{(x - x_1)^2}{2\tau}, \quad y - y_1 = (x - x_1)z_1. \quad (5.2)$$

Integration over x_1 , and then over z_1 , gives

$$I_\zeta^T = P_T \exp(P_T) \int_0^\infty \frac{\operatorname{erfc}\sqrt{P_T(1+\omega)}}{\sqrt{\omega}(1+\omega)} d\omega.$$

Here, we take into account that [67]

$$\int_0^\infty \frac{\exp(-\mu^2 u^2)}{u^2 + \beta^2} du = \frac{\pi}{2\beta} \operatorname{erfc}(\beta\mu) \exp(\beta^2 \mu^2). \quad (5.3)$$

The next step is to differentiate and integrate I_ζ^T with respect to its parameter $\sqrt{P_T}$ with allowance for

$$\int_1^\infty \frac{\exp(-\mu u)}{\sqrt{u-1}} du = \sqrt{\frac{\pi}{\mu}} \exp(-\mu). \quad (5.4)$$

As a result, we arrive at the Ivantsov solution describing the liquid undercooling Δ for a paraboloid of revolution [33,70,71],

$$I_\zeta^T = \Delta = P_T \exp(P_T) \int_1^\infty \frac{\exp(-P_T\eta)}{\eta} d\eta. \quad (5.5)$$

Combining the obtained equations (5.1) and (5.5), we are able to write down the generalized solution that is valid for the two- and three-dimensional cases

$$I_\zeta^T = \Delta = P_T \exp(P_T) I_T(\infty), \quad I_T(\eta) = \int_1^\eta \frac{\exp(-P_T v)}{v^j} dv, \quad (5.6)$$

where $j = \frac{1}{2}$ for two-dimensional and $j = 1$ for three-dimensional geometries.

In this case of the thermo-chemical Ivantsov solutions, we formally replace P_C by P_T in integrals (2.23) and (2.24) and keep in mind the concentration factor $(1 - k_0)C_i$. Hence, we get

$$I_\zeta^C = (1 - k_0)C_i P_C \exp(P_C) I_C(\infty), \quad I_C(\eta) = \int_1^\eta \frac{\exp(-P_C v)}{v^j} dv. \quad (5.7)$$

By means of further substitution of I_ζ^C into equations (2.21) and (2.22) at $d_c = 0$, $\beta = 0$ and $\partial \zeta / \partial t = 0$, we arrive at the familiar interfacial concentration [71]

$$C_i = \frac{C_{l\infty}}{1 - (1 - k_0)P_C \exp(P_C) I_C(\infty)}. \quad (5.8)$$

Expressions (5.1)–(5.8) describe the thermo-chemical propagation of a parabolic platelet or paraboloid of revolution with a constant velocity (for details, see [72]). The aforementioned equations for interface motion (2.13)–(2.15) and (2.22)–(2.24), as a consequence, contain the steady-state Ivantsov solutions so that

$$-\frac{Q}{mc_p} \left[\Delta - \frac{d_c}{\rho} K - \beta V - P_T \exp(P_T) I_T(\infty) \right] = \frac{C_{l\infty}}{1 - (1 - k_0)P_C \exp(P_C) I_C(\infty)}. \quad (5.9)$$

Finally, the temperature and solute diffusion fields in liquid around the growing parabolic platelet (two dimensions) and paraboloid of revolution (three dimensions) are

$$\left. \begin{aligned} T(\eta) &= T_f + (T_\infty - T_f) \frac{I_T(\eta)}{I_T(\infty)} \\ \text{and} \quad C_l(\eta) &= C_i + (C_{l\infty} - C_i) \frac{I_C(\eta)}{I_C(\infty)}. \end{aligned} \right\} \quad (5.10)$$

(b) Solutions for the hyperbolic equation of mass transport

Let us now consider the question of how to obtain the steady-state interfacial concentration at the parabolic platelet and paraboloid of revolution in the case of hyperbolic mass transport. This problem was considered in [68,73]. This derivation leans upon equations (3.10), (4.6) and (4.7) and the following auxiliary expression [67]:

$$K_v(xz) = \frac{z^v}{2} \int_0^\infty \exp\left(-\frac{x\alpha}{2} - \frac{xz^2}{2\alpha}\right) \alpha^{-v-1} d\alpha.$$

Again, in the two-dimensional case we introduce the new variable $\omega = (x - x_1)/\alpha$, integrate over x_1 and arrive at the integral, which is independent of x . In the three-dimensional case, $\mathbf{x} = (x, y)$ and $\mathbf{x}_1 = (x_1, y_1)$; we additionally introduce the second variable $z_1 = (y - y_1)/(x - x_1)$, and integrate over x_1 and z_1 . Omitting mathematical details, we have

$$I_\zeta^{\text{CH}} = (1 - k_v(V))P_C \exp(P_C) C_i I_C, \quad I_C = \int_1^\infty \frac{\exp(-P_C \eta)}{\eta^j} d\eta, \quad (5.11)$$

where $j = \frac{1}{2}$ and $j = 1$ for the two-dimensional and three-dimensional geometries, respectively.

The interfacial solute concentration can be found from expressions (3.10) and (5.11) as [47,68]

$$C_i = \begin{cases} \frac{C_{l\infty}}{1 - (1 - k_v(V))P_C \exp(P_C) I_C}, & W < 1, \\ C_{l\infty}, & W \geq 1. \end{cases} \quad (5.12)$$

The solid/liquid interface therewith moves in accordance with expression (4.8), where the integrals I_ζ^T and I_ζ^{CH} are determined in (5.6) and (5.11).

The concentration integrals (4.6) and (4.7) at $P_C \tau_* = W^2 = 1$ become zero and the Green functions (3.8) and (3.9) turn to zero in the case $W > 1$. This implies that $I_\zeta^{\text{CH}} = 0$ and $C_i = C_{l\infty}$ in accordance with expression (3.10). By this we mean that the concentration profile is constant (diffusionless solidification) ahead of the phase interface when the interface velocity V is equal to or greater than the diffusive speed V_D [47]. Expressions (5.12) coincide with those previously

found by means of the Ivantsov and Horvay–Cahn methods [68,73] for hyperbolic mass transport. Solutions (5.11) and (5.12) are correct only in some area behind the dendrite tip. Far from the tip, in the region where the undercooling may be much smaller than at the tip, the dendrite velocity can be lower than the diffusion speed, $V \ll V_D$, $W \ll 1$. In such a case, the dendrite may grow under local equilibrium conditions and solutions (5.11) and (5.12) transform to the classical Ivantsov solutions obtained using the parabolic transport equations [70,71].

6. Steady-state Horvay–Cahn solutions

A number of experimental data show that in many cases the growing shapes of dendrites are non-symmetric. For instance, ice crystals evolving in pure water and in water–ethyleneglycol solution or dendritic evolution in aluminium nitride, lithium niobate or lithium tantalate represent several examples of the sixfold symmetry which is caused by the hexagonal crystalline anisotropy [4,5,74–78]. In these cases, dendritic shapes do not satisfy the Ivantsov solutions [70,71] and one must use the Horvay–Cahn solutions characterizing possible lower symmetric dendritic shapes [79–81]. In this section, we demonstrate how to derive their analytical solutions from the boundary integral theory.

(a) Parabolic heat and mass transfer equations

Horvay & Cahn [79] showed that the shape of a growing dendrite can be an elliptical cross section, such that the dendritic surface in dimensionless variables is given by

$$\frac{x^2}{\omega - a} + \frac{y^2}{\omega + a} = \omega - 2z, \quad (6.1)$$

where $2D_T/V = \rho/P_T$ is the length scale and ρ represents the dendrite tip diameter of any of its cross sections (or the average value of the dendritic tip curvature radii). The dendrite interface is described by $\omega = P_T$ and a represents the aspect ratio of the elliptical cross section of the dendrite. The cross section is circular if $a = 0$ ($|a| < P_T$). Equation (6.1) represents a symmetrized case of the corresponding Horvay–Cahn equation, keeping in mind the dimensionless radii of curvature $P_T - a$ in the x - z plane and $P_T + a$ in the y - z plane. Thus, the average dimensionless radius of curvature is P_T [80].

In dimensional form, expression (6.1) becomes

$$\frac{x_d^2}{\omega_d - a_d} + \frac{y_d^2}{\omega_d + a_d} = \omega_d - 2z_d, \quad (6.2)$$

where $\omega_d = \omega\rho/P_T$ and $a_d = a\rho/P_T$, and the subscript d designates the dimensional variables and parameters. The dimensionless interface function and undercooling are determined by expressions (2.13) and (2.15).

In the steady-state propagation of an elliptical paraboloid into an undercooled liquid with constant velocity V ($\partial\zeta/\partial t = 0$), equation (2.15) reads

$$I_{\zeta d}^T = \left(\frac{P_T}{2\pi\rho}\right)^{3/2} \frac{1}{\sqrt{V}} \int_0^\infty \frac{d\tau}{\tau^{3/2}} \int_{-\infty}^\infty \int_{-\infty}^\infty d^2x_1 \\ \times \exp \left\{ -\frac{P_T}{2\tau} \frac{1}{\rho V} [|\mathbf{x} - \mathbf{x}_1|^2 + (\zeta(\mathbf{x}) - \zeta(\mathbf{x}_1) + \tau V)^2] \right\}. \quad (6.3)$$

This equation can be rewritten by means of expression (6.2) as

$$I_{\zeta d}^T = \left(\frac{P_T}{2\pi\rho}\right)^{3/2} \frac{1}{\sqrt{V}} \int_0^\infty \frac{d\tau}{\tau^{3/2}} \int_{-\infty}^\infty \int_{-\infty}^\infty \exp \left\{ -\frac{P_T}{2\tau} \frac{1}{\rho V} \left[(x - x_1)^2 + (y - y_1)^2 \right. \right. \\ \left. \left. + \left(\frac{x_1^2 - x^2}{2(\omega_d - a_d)} + \frac{y_1^2 - y^2}{2(\omega_d + a_d)} + \tau V \right)^2 \right] \right\} dx_1 dy_1. \quad (6.4)$$

Now, replacing the integration variables τ and y_1 by ω_1 and z_1 , respectively, using equation (5.2), we arrive at

$$I_{\zeta d}^T = \left(\frac{P_T}{\pi\rho}\right)^{3/2} \frac{1}{2\sqrt{V}} \int_0^\infty \frac{d\omega_1}{\sqrt{\omega_1}} \int_{-\infty}^\infty \exp\left(-\frac{P_T\omega_1}{\rho V}(1+z_1^2)\right) dz_1 \\ \times \int_{-\infty}^\infty \exp\left\{-\frac{P_T\omega_1}{\rho V} \left(-\frac{x_1+x}{2(\omega_d-a_d)} - \frac{z_1(2y-z_1(x-x_1))}{2(\omega_d+a_d)} + \frac{V(x-x_1)}{2\omega_1}\right)^2\right\} dx_1. \quad (6.5)$$

Integrating the right-hand side of expression (6.5) over x_1 , we get

$$I_{\zeta d}^T = \frac{P_T(\omega_d+a_d)}{\pi\rho} \int_0^\infty \frac{1}{\omega_1} \exp\left(-\frac{P_T\omega_1}{\rho V}\right) d\omega_1 \int_{-\infty}^\infty \frac{\exp(-P_T\omega_1 z_1^2/\rho V) dz_1}{z_1^2 + (\omega_d+a_d)(V/\omega_1 + 1/(\omega_d-a_d))}. \quad (6.6)$$

The next step is to integrate the right-hand side of equation (6.6) over z_1 taking into account the integral expression (5.4) as

$$I_{\zeta d}^T = \frac{P_T\sqrt{\omega_d+a_d}}{\rho} \int_0^\infty \frac{\exp((P_T/V\rho)(\omega_d+a_d)(V+\omega_1/(\omega_d-a_d))) - P_T\omega_1/V\rho}{\sqrt{\omega_1}\sqrt{V+\omega_1/(\omega_d-a_d)}} \\ \times \operatorname{erfc}\left(\sqrt{\frac{P_T}{V\rho}(\omega_d+a_d)}\left(V+\frac{\omega_1}{\omega_d-a_d}\right)\right) d\omega_1. \quad (6.7)$$

Replacing variable ω_1 by $u = (1/\sqrt{V})\sqrt{V+\omega_1/(\omega_d-a_d)}$, we have

$$I_{\zeta d}^T = \frac{2P_T}{\rho} \sqrt{\omega_d^2 - a_d^2} \exp\left[\frac{P_T}{\rho}(\omega_d - a_d)\right] J(\omega_d), \quad (6.8)$$

where

$$J(\omega_d) = \int_1^\infty \frac{\exp((P_T/\rho)2a_d u^2) \operatorname{erfc}(u\sqrt{(P_T/\rho)(\omega_d+a_d)}) du}{\sqrt{u^2-1}}. \quad (6.9)$$

Using the method of differentiation and integration of $J(\omega_d)$, we have

$$I_{\zeta d}^T = \frac{P_T}{\rho} \sqrt{\omega_d^2 - a_d^2} \exp\left(\frac{P_T\omega_d}{\rho}\right) \int_{\omega_d}^\infty \frac{\exp(-(P_T/\rho)t) dt}{\sqrt{t^2 - a_d^2}}. \quad (6.10)$$

At the interface, $\omega_d = \rho$, we get

$$I_{\zeta d}^T = \sqrt{P_T^2 - a_d^2} \frac{P_T^2}{\rho^2} \exp(P_T) G(P_T), \quad (6.11)$$

where

$$G(P_T) = \int_{P_T}^\infty \frac{\exp(-y) dy}{\sqrt{y^2 - a_d^2(P_T^2/\rho^2)}} \quad (6.12)$$

and

$$\frac{c_p(T_f - T_\infty)}{Q} = I_{\zeta d}^T. \quad (6.13)$$

Expression (6.13) for the melt undercooling $\Delta = (T_f - T_\infty)/T_Q$ gives a relation between the unknown dendritic parameters ρ and V . The present solution (6.11) transforms to the Horvay–Cahn twofold solution [80] after transition to the dimensionless parameter $a = a_d P_T/\rho$

$$I_\zeta^T = I_{\zeta d}^T = \sqrt{P_T^2 - a^2} \exp(P_T) \int_{P_T}^\infty \frac{\exp(-y) dy}{\sqrt{y^2 - a^2}}. \quad (6.14)$$

It is important to note that the case of the circular cross section, $a=0$, gives the Ivantsov solution [70,71].

The dimensional Horvay–Cahn temperature distribution in liquid has the form [79–81]

$$\left. \begin{aligned} T(\omega) &= T_{pi} + (T_{pi} - T_{\infty}) \frac{G(\omega) - G(P_T)}{G(P_T)} \\ T_{pi} &= T_{\infty} + T_Q \sqrt{P_T^2 - a^2} \exp(P_T) G(P_T). \end{aligned} \right\} \quad (6.15)$$

and

The Horvay–Cahn-type solution for the thermo-chemical problem can be found by analogy with the temperature problem (6.3)–(6.15). Using similarity between the thermal and concentration problems, we have

$$I_{\xi}^C = I_{\xi d}^C = (1 - k_0) C_i \sqrt{P_C^2 - a^2} \exp(P_C) \int_{P_C}^{\infty} \frac{\exp(-y) dy}{\sqrt{y^2 - a^2}} \quad (6.16)$$

and

$$\left. \begin{aligned} C_1(\omega) &= C_i + (C_i - C_{l\infty}) \frac{G_C(\omega) - G_C(P_C)}{G_C(P_C)} \\ C_i &= \frac{C_{l\infty}}{1 - (1 - k_0) \sqrt{P_C^2 - a^2} \exp(P_C) G_C(P_C)}, \quad G_C(P_C) = \int_{P_C}^{\infty} \frac{\exp(-y) dy}{\sqrt{y^2 - a^2}}. \end{aligned} \right\} \quad (6.17)$$

The function $\omega = \omega(x, y, z)$ is given by equation (6.1). This equation has three roots, but only one of them is positive for all possible values of parameters. This root is found from the Cardano formula

$$\omega(x, y, z) = \frac{2z}{3} + \sqrt[3]{\frac{-q_{\omega} + \sqrt{q_{\omega}^2 + 4p_{\omega}^3/27}}{2}} + \sqrt[3]{\frac{-q_{\omega} - \sqrt{q_{\omega}^2 + 4p_{\omega}^3/27}}{2}}, \quad (6.18)$$

where

$$q_{\omega}(x, y, z) = \frac{4}{3}za^2 - ax^2 + ay^2 - \frac{16}{27}z^3 - \frac{2}{3}z(x^2 + y^2) \quad (6.19)$$

and

$$p_{\omega}(x, y, z) = -\left(\frac{4}{3}za^2 + a^2 + x^2 + y^2\right). \quad (6.20)$$

Analysing the Horvay–Cahn solutions [80], it is suitable to use the parabolic coordinates (ξ, η, φ) connected with the Cartesian ones (x, y, z) as

$$x = \xi \eta \cos \varphi, \quad y = \xi \eta \sin \varphi \quad \text{and} \quad z = \frac{1}{2}(\xi^2 - \eta^2). \quad (6.21)$$

The dendritic shape steadily growing in the z -direction as an elliptical paraboloid is described in the parabolic frame of reference by

$$\xi^2 \eta^2 \left[\frac{\cos^2 \varphi}{\omega - a} + \frac{\sin^2 \varphi}{\omega + a} \right] = \omega - \xi^2 + \eta^2. \quad (6.22)$$

This expression determines ω as a function of (ξ, η, φ) in the form

$$\omega(\xi, \eta, \varphi) = \frac{\xi^2 - \eta^2}{3} + \sqrt[3]{\frac{-q_1 + \sqrt{q_1^2 + 4p_1^3/27}}{2}} + \sqrt[3]{\frac{-q_1 - \sqrt{q_1^2 + 4p_1^3/27}}{2}}, \quad (6.23)$$

where

$$q_1(\xi, \eta, \varphi) = \frac{2(\eta^2 - \xi^2)^3}{27} + \frac{(\eta^2 - \xi^2)(a^2 + \xi^2 \eta^2)}{3} + a^2(\xi^2 - \eta^2) - \xi^2 \eta^2 a(\cos^2 \varphi - \sin^2 \varphi) \quad (6.24)$$

and

$$p_1(x, y, z) = -\left(\xi^2 \eta^2 + a^2 + \frac{(\eta^2 - \xi^2)^2}{3}\right). \quad (6.25)$$

Thus, the Horvay–Cahn solutions completely follow from the boundary integral theory. The thermo-solutal parabolic problem within the Horvay–Cahn formalism is described by expressions (2.21) and (6.14)–(6.17).

(b) Parabolic heat and hyperbolic mass transfer equations

Replacement of the variable z by z_h ,

$$z_h = z \sqrt{1 - \frac{V^2}{V_D^2}}, \quad (6.26)$$

in the parabolic solute transport equation leads to the hyperbolic equation taking into account the finite speed V_D of atomic diffusion [73]. Defining $\sqrt{1 - V^2/V_D^2} = C_h$, we get the average tip diameter, chemical Péclet number and elliptical paraboloid equation (6.2) as

$$\left. \begin{aligned} \rho_{\text{new}} &= \frac{\rho}{C_h}, \quad P_C^* = \frac{\rho_{\text{new}} V}{2D_C} = \frac{P_C}{C_h} \\ \text{and} \quad \zeta_{dh} &= \frac{\sqrt{1 - V^2/V_D^2}}{2} \left(\omega_d - \frac{x_d^2}{\omega_d - a_d} - \frac{y_d^2}{\omega_d + a_d} \right) \end{aligned} \right\} \quad (6.27)$$

The integral equation of the interface motion in dimensionless form is given by equation (4.8), where I_ζ^C reads as (see equations (4.6) and (4.7) and the discussion around them)

$$\left. \begin{aligned} I_\zeta^{\text{CH}} &= P_C^{3/2} \int_0^\infty \frac{d\tau}{(2\pi\tau)^{3/2}} \int_{-\infty}^\infty \int_{-\infty}^\infty d^2x_1 (1 - k_v(v)) C_i(\mathbf{x}_1, t - \tau) \left[1 + \frac{\partial \zeta(\mathbf{x}_1, t - \tau)}{\partial t} \right] \\ &\quad \times \exp \left\{ -\frac{P_C}{2\tau} \left[|\mathbf{x} - \mathbf{x}_1|^2 + (\zeta(\mathbf{x}, t) - \zeta(\mathbf{x}_1, t - \tau) + \tau)^2 \right] \right\}, \quad W < 1, \\ I_\zeta^{\text{CH}} &= 0, \quad W \geq 1. \end{aligned} \right\} \quad (6.28)$$

Further, in this section we consider only the case of velocity which is smaller than the diffusion speed, i.e. $W < 1$, $V < V_D$.

Returning to the dimensional coordinates and assuming that the elliptical paraboloid does not change its shape and moves with constant velocity V (i.e. $\dot{\zeta} = 0$), we get from equation (6.28) that

$$\begin{aligned} I_{\zeta d}^{\text{CH}} &= (1 - k_v(V)) \left(\frac{P_C}{2\pi\rho} \right)^{3/2} \frac{C_i}{\sqrt{V}} \int_0^\infty \frac{d\tau}{\tau} \tau^{3/2} \int_{-\infty}^\infty \int_{-\infty}^\infty \exp \left\{ -\frac{P_C}{2\tau} \frac{1}{\rho V} \left[(x - x_1)^2 + (y - y_1)^2 \right. \right. \\ &\quad \left. \left. + \left(C_h \frac{x_1^2 - x^2}{2(\omega_d - a_d)} + C_h \frac{y_1^2 - y^2}{2(\omega_d + a_d)} + \tau V \right)^2 \right] \right\} dx_1 dy_1. \end{aligned} \quad (6.29)$$

Replacing two integration variables τ and y_1 by ω_1 and z_1 , respectively, defined by equation (5.2), we obtain

$$\begin{aligned} I_{\zeta d}^{\text{CH}} &= (1 - k_v(V)) \left(\frac{P_C}{2\pi\rho} \right)^{3/2} \frac{C_i}{\sqrt{V}} \int_0^\infty \frac{d\omega_1}{\sqrt{\omega_1}} \int_{-\infty}^\infty \exp \left(-\frac{P_C \omega_1}{\rho V} (1 + z_1^2) \right) dz_1 \\ &\quad \times \int_{-\infty}^\infty \exp \left\{ -\frac{P_C \omega_1}{2\rho V} \left(-C_h \left(\frac{x_1 + x}{\omega_d - a_d} + \frac{z_1(2y - z_1(x - x_1))}{\omega_d + a_d} \right) + \frac{V(x - x_1)}{\omega_1} \right)^2 \right\} dx_1. \end{aligned} \quad (6.30)$$

Now, replacing the integration variable x_1 by $\tilde{\alpha}$,

$$\tilde{\alpha} = \sqrt{\frac{P_C \omega_1}{2\rho V}} \left(-C_h \left(\frac{x_1 + x}{\omega_d - a_d} + \frac{z_1(2y - z_1(x - x_1))}{\omega_d + a_d} \right) + \frac{V(x - x_1)}{\omega_1} \right), \quad (6.31)$$

and integrating the right-hand side of equation (6.30) over $\tilde{\alpha}$, we get

$$\begin{aligned} I_{\zeta d}^{\text{CH}} &= (1 - k_v(V)) C_i \frac{P_C}{C_h} \frac{\omega_d + a_d}{\pi\rho} \\ &\quad \times \int_0^\infty \frac{\exp(-P_C \omega_1 / \rho V) d\omega_1}{\omega_1} \int_{-\infty}^\infty \frac{\exp(-P_C \omega_1 z_1^2 / \rho V) dz_1}{z_1^2 + ((\omega_d + a_d)/C_h)(V/\omega_1 + C_h/(\omega_d - a_d))}. \end{aligned} \quad (6.32)$$

Integrating the right-hand side of equation (6.32) over z_1 and taking into account equation (5.4), we evaluate the chemical integral (6.31) as

$$I_{\zeta d}^{\text{CH}} = \frac{P_C}{\rho C_h} (1 - k_v(V)) C_i \sqrt{\omega_d + a_d} \int_0^\infty \frac{\exp((P_C/V\rho)(\omega_d + a_d)(V/C_h + \omega_1/(\omega_d - a_d)) - P_C\omega_1/V\rho)}{\sqrt{\omega_1} \sqrt{V/C_h + \omega_1/(\omega_d - a_d)}} \times \operatorname{erfc} \left(\sqrt{\frac{P_C}{V\rho}(\omega_d + a_d)} \left(\frac{1}{C_h} + \frac{\omega_1}{\omega_d - a_d} \right) \right) d\omega_1. \quad (6.33)$$

Replacing ω_1 by $u = \sqrt{1 + \omega_1 C_h/V(\omega_d - a_d)}$, we obtain

$$I_{\zeta d}^{\text{CH}} = 2(1 - k_v(V)) C_i \frac{P_C}{\rho C_h} \sqrt{\omega_d^2 - a_d^2} \exp \left(\frac{P_C}{\rho C_h} (\omega_d - a_d) \right) J_{\text{CH}}(\omega_d), \quad (6.34)$$

where

$$J_{\text{CH}}(\omega_d) = \int_1^\infty \frac{\exp((P_C/\rho C_h)2a_d u^2) \operatorname{erfc}(u \sqrt{(P_C/\rho C_h)(\omega_d + a_d)}) du}{\sqrt{u^2 - 1}}. \quad (6.35)$$

Further, applying the method of differentiation and integration of $J_{\text{CH}}(\omega_d)$, we get

$$I_{\zeta d}^{\text{CH}} = (1 - k_v(V)) C_i \frac{P_C}{\rho C_h} \sqrt{\omega_d^2 - a_d^2} \exp \left(\frac{P_C \omega_d}{\rho C_h} \right) \int_{\omega_d}^\infty \frac{\exp(-P_C/\rho C_h t) dt}{\sqrt{t^2 - a_d^2}}. \quad (6.36)$$

At the interface, $\omega_d = \rho$, one obtains

$$I_{\zeta d}^{\text{CH}} = (1 - k_v(V)) C_i \sqrt{P_C^{*2} - a_d^2 \frac{P_C^{*2}}{\rho^2}} \exp(P_C^*) G_c(P_C^*), \quad (6.37)$$

where

$$G_c(P_C^*) = \int_{P_C^*}^\infty \frac{\exp(-y) dy}{\sqrt{y^2 - a_d^2 P_C^{*2}/\rho^2}}. \quad (6.38)$$

Expressions (6.37) and (6.38) transform to equation (5.11) in the limiting case $a_d = 0$ of the circular paraboloid. Note that integral (6.37) is identical to integral (6.16) in the case of the parabolic mass transfer mechanism when $V \ll V_D$, $P_C^* \rightarrow P_C$ and a tends to $a_d P_C/\rho$. The concentration distribution in the present case is given by expressions (6.17) when P_C is replaced by P_C^* , whereas the temperature field is governed by equations (6.15).

As a final note of this section, the boundary integral theory includes the Horvay–Cahn steady-state temperature and solute concentration solutions within the framework of parabolic and hyperbolic transport equations.

7. A globular shape of dendritic tips at high Péclet numbers

In this section, we demonstrate that the solid/liquid interface, which is determined by the boundary integrals (2.13), (2.22) and (3.13), has a circular (spherical) shape in the steady-state solidification conditions with high Péclet numbers in the case of either the parabolic or hyperbolic description of transport. Setting $P_T \rightarrow \infty$ and $P_C \rightarrow \infty$, we conclude that integrals (2.14), (2.15), (2.23), (2.24) and (3.11) tend to zero, whereas conditions (2.13), (2.22) and (3.13) for the interface function become

$$K(\zeta) = B, \quad B = \frac{\rho}{d_c} \left(\Delta - \beta V + \frac{m_v C_{l\infty}}{T_Q} \right), \quad (7.1)$$

where the interface curvature K is given by expressions (2.3).

Substituting K for the two-dimensional case into (7.1), we get

$$\frac{d^2\zeta}{dx^2} + B \left[1 + \left(\frac{d\zeta}{dx} \right)^2 \right]^{3/2} = 0.$$

This equation can be easily integrated in the form

$$\zeta(x) = \zeta_0 + \frac{1}{B} \sqrt{1 - (C_0 - Bx)^2}, \quad (7.2)$$

where ζ_0 and C_0 are arbitrary constants. Equation (7.2) shows that the interface function $\zeta(x)$ represents a branch of the circle. This can be easily demonstrated by means of the squaring operation and transformation to the canonical form.

In the three-dimensional case, we have from equations (2.3) and (7.1)

$$\frac{\nabla\zeta}{\sqrt{1 + (\nabla\zeta)^2}} = (C_x + a_x x)\mathbf{i} + (C_y + a_y y)\mathbf{j}, \quad (7.3)$$

where \mathbf{i} and \mathbf{j} are the unit coordinate vectors, a_x, a_y, C_x, C_y are constants and $a_x + a_y = -B$. This equation implies

$$1 + (\nabla\zeta)^2 = \frac{1}{1 - (C_x + a_x x)^2 - (C_y + a_y y)^2}. \quad (7.4)$$

Now, integrating equation (7.3) and taking into account expression (7.4), we obtain the surface with $a_x = a_y = -B/2$ as

$$\zeta(x, y) = \zeta_0 + \frac{2}{B} \sqrt{1 - \left(C_x - \frac{Bx}{2} \right)^2 - \left(C_y - \frac{By}{2} \right)^2}. \quad (7.5)$$

Equation (7.5) describes a spherical surface similar to that of the two-dimensional geometry (7.2). Asymptotically, the boundary integral equations define the growth of spherical surfaces (or nuclei), which is caused by the constant driving force entering into the right-hand side of equation (7.1).

Now, we solve equations (7.1) and (7.5) to check the shape of the dendrite tip in the anisotropic and isotropic cases. Because the anisotropic capillary length d_c and anisotropic kinetic growth coefficient β in the three-dimensional case have the following form (see [48] and references therein):

$$d_c(\theta, \varphi) = d_0 \{1 - \alpha_d [\cos^4 \theta + \sin^4 \theta (1 - 2 \sin^2 \varphi \cos^2 \varphi)]\} \quad (7.6)$$

and

$$\beta(\theta, \varphi) = \beta_0 \{1 - \alpha_\beta [\cos^4 \theta + \sin^4 \theta (1 - 2 \sin^2 \varphi \cos^2 \varphi)]\}, \quad (7.7)$$

it is convenient to transform Cartesian coordinates to spherical coordinates defined by

$$x(\theta, \varphi) = \frac{2d_0}{\rho} \sin \theta \cos \varphi \quad \text{and} \quad y(\theta, \varphi) = \frac{2d_0}{\rho} \sin \theta \sin \varphi, \quad (7.8)$$

where α_β is the kinetic anisotropy parameter.

To obtain the growth velocity V and the tip diameter ρ in equations (7.1) and (7.5), we use the selection criterion σ^* as

$$\rho = \frac{d_0}{\sigma^* P_T} \quad \text{and} \quad V = \frac{2D_T P_T^2}{d_0} \sigma^*. \quad (7.9)$$

Because equation (7.1) has been found within the limits $P_T \rightarrow \infty$ and $P_C \rightarrow \infty$ and we have to obtain the surfaces with the finite and non-zero values of V and ρ from equation (7.9), we use σ^*

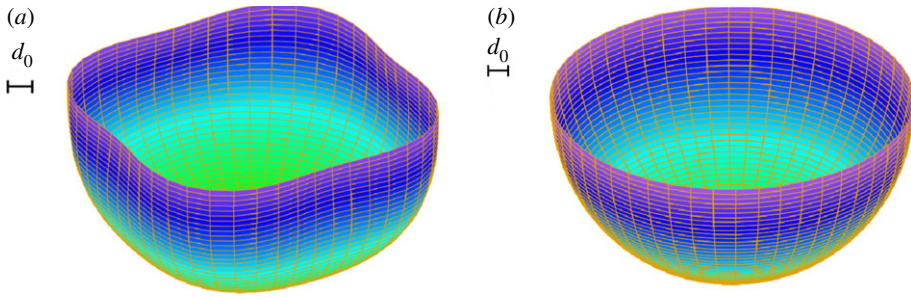


Figure 2. A globular form of dendritic tips growing from Ti-Al melt at the kinetically limited regime. Dimensionless undercooling $\Delta = 1.0$, growth Péclet number $P_T = 1$ and with an (a) anisotropic interface and (b) isotropic interface. The anisotropic globular tip is deformed in the direction of anisotropy strength and a smooth globular tip appears in the isotropic case. The scale of capillary length d_0 is shown for both figures.

from the kinetic growth mode [56],

$$\sigma^* = \frac{d_0}{2D_T P_T} \cdot \frac{\sigma_0 \alpha_\beta^{5/4} P}{\beta_0 (1 + h \sqrt{\alpha_\beta} P_T P_1 / P)}, \quad (7.10)$$

for which we merely take the large and finite value of the Péclet number $P_T = 1$. In equation (7.10), we have

$$h = \frac{d_0 \alpha_\beta^{3/4} P^2}{2D_T \beta_0 H P_1 \alpha_d^{3/4}}, \quad (7.11)$$

$$H = \frac{1}{a_1^2 (1 + \delta_0 D_T \beta_0 / d_0)^2} + \frac{2m C_{1\infty} (k_0 - 1) c_p D_C}{a_2^2 (1 + \delta_0 D_C \beta_0 / d_{0CD})^2 Q D_T} \quad (7.12)$$

and

$$P_1 = 1 + \frac{2m C_{1\infty} (k_0 - 1) c_p D_T^2}{(Q D_C^2)}, \quad P = 1 + \frac{2m C_{1\infty} (k_0 - 1) c_p D_T}{(Q D_C)} \quad (7.13)$$

and $d_{0CD} = T_Q d_0 / (2m C_{1\infty} (k_0 - 1))$. The constants a_1 , a_2 and δ_0 are given by

$$a_1 = \left(\frac{8\sigma_0}{7} \right)^{1/2} \left(\frac{3}{56} \right)^{3/8}, \quad a_2 = \sqrt{2} a_1 \quad \text{and} \quad \delta_0 = 20 \sqrt{\frac{7}{24}} \left(\frac{56}{3} \right)^{3/8}. \quad (7.14)$$

For the computation of shapes by equations (7.1) and (7.5) using equations (7.9)–(7.14), we have the chosen material parameters of an Ti-Al alloy given in table 1. The calculations have been made for the steady-state growth at the dimensionless undercooling $\Delta = 1$. The results of calculations are shown in figure 2, which demonstrates the areas around the dendrite tips in the anisotropic (a) and isotropic (b) cases. At the large value of the Péclet number, $P_T = 1$, chosen in calculations, these shapes are qualitatively consistent with the globular shape appearing at the high-growth regimes of crystal formation [83–87]. Computations by the phase-field model of Karma & Rappel [88] showed that the crystal growth morphology also exhibits non-branching shapes of a globular form at very high undercooling [89]. Even though the characteristic scales of patterns of figures 2 and 3 are different ($d_0 \ll 10D_T/V$), these crystal shapes have a clear qualitative similarity: the deformed semi-sphere (figure 2a) has a similarity to the anisotropic spherical globe (figure 3a), and the spherical tip of the dendrite (figure 2b) is similar to the isotropic spherical globe (figure 3b). From this it follows that the solution (7.5) describes the globular tips of dendrites qualitatively consistent with the results of phase-field modelling for high growth rates of crystals.

With regard to the comparison of patterns reproduced by the boundary integral method (figure 2) and the phase-field model (figure 3), a natural question arises about the preferable applicability of these approaches depending on the modelled system and length scales. Indeed,

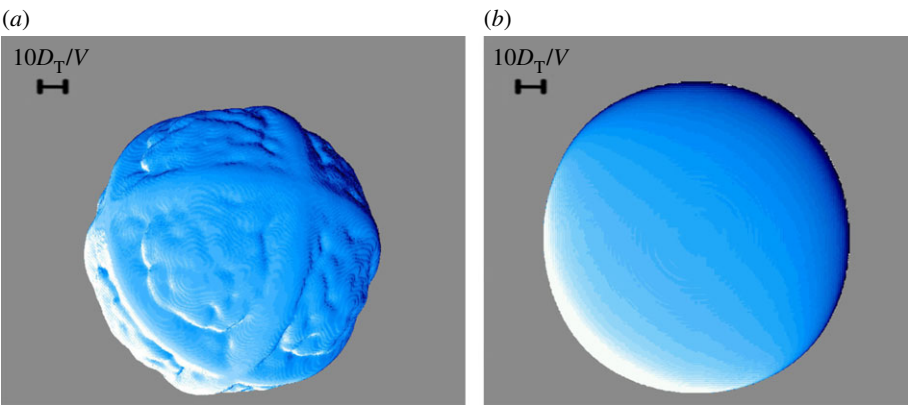


Figure 3. Globular shapes of crystals from a morphological spectrum of crystals [89] obtained by the phase-field model of Karma & Rappel [88]. Computations were made for nickel crystals growing with (a) the anisotropic interface at the dimensionless undercooling $\Delta = 1.1$ and (b) the isotropic interface at the dimensionless undercooling $\Delta = 1.2$. The scale of 10 thermal lengths $10D_T/V$ is shown for both figures.

Table 1. Material parameters of a Ti–Al alloy (mainly taken from [82]).

| parameter | | | | value |
|------------------------------------|----------------|----------------------------|--|------------------------|
| nominal concentration | C_{∞} | at. % | | 35 |
| adiabatic temperature | T_Q | K | | 273 |
| thermal diffusivity | D_T | $\text{m}^2 \text{s}^{-1}$ | | 7.5×10^{-6} |
| capillary constant | d_0 | m | | 9.28×10^{-10} |
| liquidus slope | m | K/at. % | | −8.78 |
| partition coefficient | k_0 | — | | 0.86 |
| kinetic coefficient | β_0 | s m^{-1} | | 1.88×10^{-2} |
| stability constant | σ_0 | — | | 0.1 |
| strength of the kinetic anisotropy | α_β | — | | 0.5 |
| diffusion coefficient | D_C | $\text{m}^2 \text{s}^{-1}$ | | 5.27×10^{-9} |

the phase-field model is a well-established thermodynamically consistent method, which is nowadays developed for many multi-component and multi-phase systems (see [57] and references therein). It must be applied to the transformations and reactions in which the diffuse interface between different states plays a specific role [90,91]. In solidification processes, the diffuse interface has a width of several lattice parameters and a whole pattern, which can be computationally reproduced by the phase-field model, and has a scale from several microns to fractions of millimetres. The boundary integral method is based on the sharp interface formulation in which the thickness of the interface is negligibly small, i.e. it has zero width. Owing to this feature, the boundary integral method may cover macro-scales (up to metres in lengths), for instance in modelling of dendrites and grains growing or melting in the Arctic sea. In addition to this, it can reproduce the dendritic pattern much faster than the phase-field method. Therefore, patterns modelled by the boundary integral method may be used as the first benchmarks for the phase-field model, which can then be used for more precise solutions.

Concluding this section, one has to remark that equation (7.1) represents the Gibbs–Thomson condition in the limit of infinite Péclet numbers. A consistency of such a limiting case with the

velocity and acceleration-dependent Gibbs–Thomson equation [92] would be a subject of further analysis.

8. Computational modelling

(a) Model equations

Neglecting the concentration gradient in solid, $\nabla C_S = 0$, let us introduce concentration $u(r) = C_i(r) - C_{1\infty}$, where $C_i(r)$ is the concentration at the interface and $C_{1\infty} = \text{const}$ is the concentration of a solute at infinity. All analytical treatments as well as all numerical approximations are made in the dimensionless coordinates

$$\frac{z}{h_D \sqrt{1 - W^2}} \rightarrow z \quad \text{and} \quad \frac{x}{h_D} \rightarrow x, \quad (8.1)$$

where $h_D = D_C/V_D$ is the length scale for inter-diffusion.

We shall model a two-dimensional dendrite shape under steady conditions with constant interface velocity. Then, the diffusion mass transport in the region Ω (figure 4) in coordinates (8.1) is described by

$$\left(\frac{\partial^2}{\partial x^2} + \frac{\partial^2}{\partial z^2} \right) X + \frac{W}{\sqrt{1 - W^2}} \frac{\partial}{\partial z} X = 0. \quad (8.2)$$

Substitution of the concentration (3.10) with the integral (4.6) into the mass balance (3.2) gives the equation

$$(1 - k_v(W_n))C_i W_n = -\sqrt{1 - W^2} \frac{\partial C_i}{\partial n}, \quad (8.3)$$

for the steadily propagating interface, where the normal n is directed from the solid to the liquid. Then, the boundary integral for the steady interface takes the following form:

$$\int_{\zeta_{SL}} d\zeta_i g(r - r') \frac{\partial u(r)}{\partial n} = \int_{\zeta_{SL}} d\zeta_i h(r - r') u(r), \quad (8.4)$$

with ζ_i the whole interfacial contour, including the phase interface ζ_{SL} and boundaries of the computational domain shown in figure 4. In equation (8.4), we have

$$g(r - r') = \frac{1}{2\pi} \exp[P_C^*(z - z')] K_0(P_C^*|r - r'|), \quad (8.5)$$

the Green function of the operator

$$L^+ = \nabla^2 - \frac{W}{\sqrt{1 - W^2}} \frac{\partial}{\partial z}$$

(because one gets $L^+ g(r - r') = -\delta(r - r')$), and

$$\begin{aligned} h(r - r') &= \frac{\partial g(r - r')}{\partial n} - 2P_C^* n_z g(r - r') - \alpha(r') \delta(r - r') = -\alpha(r') \delta(r - r') \\ &+ \frac{P_C^*}{2\pi} \exp[P_C^*(z - z')] \left(-n_z K_0(P_C^*|r - r'|) - \frac{n \cdot (r - r')}{|r - r'|} K_1(P_C^*|r - r'|) \right) \end{aligned} \quad (8.6)$$

the kernel. Here, K_0 and K_1 are the modified Bessel functions of the zero and first order, respectively,

$$|r - r'| = \sqrt{(x - x')^2 + (z - z')^2} \quad (8.7)$$

is the norm in the two-dimensional domain, and

$$P_C^* = \frac{P_C}{\sqrt{1 - W^2}} = \frac{V\rho}{2D\sqrt{1 - W^2}} \quad (8.8)$$

is the modified Péclet number for the inter-diffusion, which depends on the ratio $W = V/V_D$ between the interface velocity V and the maximum diffusion speed V_D .

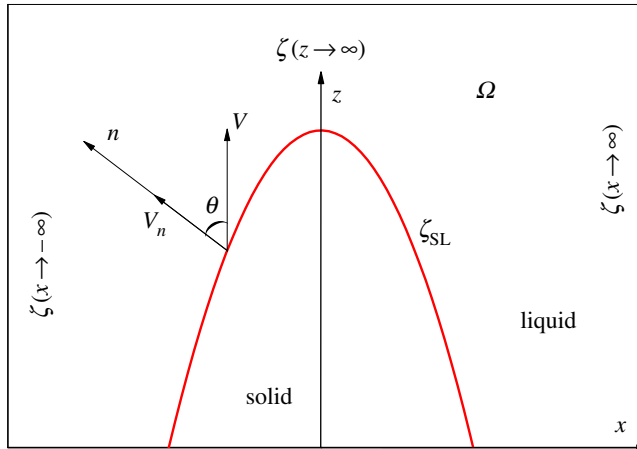


Figure 4. A schematic view of the two-dimensional domain with the solid/liquid interface ζ_{SL} propagating in the direction of the z -axis.

The boundary integral (8.4) is obtained for $W = V/V_D = \text{const}$, and it is considered as the equation for the normal gradient of concentration, $\partial u(r)/\partial n$, which drives the interface. Equation (8.4) and expressions (8.5)–(8.8) are true for an interface velocity smaller than the diffusion speed, i.e. at $W < 1$, $V < V_D$. If the interface moves with a velocity equal to or greater than the solute diffusion speed, $W \geq 1$, $V \geq V_D$, diffusionless growth with $C_i(r) = C_{i\infty}$, $u(r) = 0$ occurs [60,63], and both sides of the boundary integral equation (8.4) are reduced to zero (see also steady-state solutions (4.6) and (4.7) and the discussion around them). A boundary integral that is consistent with the analytical results does not exist [68]: for the case $W \geq 1$, $V \geq V_D$, an arbitrary crystal shape is possible in the isothermally solidified binary mixture. Finally, in the local equilibrium limit, $W \ll 1$, $V \ll V_D$, equations (8.4)–(8.8) are reduced to the previously known boundary integral of Saito *et al.* [31], obtained for the analysis of dendrite shape selection.

In what follows, we shall need one of the features of equation (8.6), namely

$$\oint_{\zeta_i} d\zeta_i h(r - r') = 0. \quad (8.9)$$

Condition (8.9) appears if we substitute the simplest solution, $u(r) = \text{const}$, of equation (8.2) into

$$\oint_{\zeta_i} d\zeta_i g(r - r') \frac{\partial u(r)}{\partial n} = \oint_{\zeta_i} d\zeta_i h(r - r') u(r), \quad (8.10)$$

which includes the whole contour ζ_i of the domain Ω (figure 4), and generalizes the boundary integral (8.4). Such substitution is correct because the function $h(r - r')$ depends not on the form of the solution but on the shape of the interface ζ_i .

The kernel (8.6) has the constant $\alpha(r')$, which is obtained by integration of the delta function along the phase interface,

$$\alpha(r') = \iint_{\Omega} \delta(r - \zeta_i(r)) d\Omega, \quad (8.11)$$

where $r' = \zeta_i(r)$ is the equation of the complete interface and Ω is the liquid region enclosed by the boundary ζ_i , i.e. the region enclosed by the solid/liquid interface ζ_{SL} and three infinite lines defined by $x \rightarrow +\infty$, $x \rightarrow -\infty$ and $z \rightarrow \infty$ (figure 4). For instance, if the interface is a circle with radius R_0 , then $r' = R_0$ is the polar coordinate (scalar) that gives

$$\alpha(r') = \int_0^{2\pi} d\phi \int_0^\infty \delta(r - R_0) r dr = 2\pi R_0. \quad (8.12)$$

The constant $\alpha(r')$ appears due to the fact that the argument of the delta function has a null value not in one point (for which the constant $\alpha(r') = 1$) but on some manifold. In our case, this manifold is represented by the one-dimensional curve (given by the interface) as well as at infinite points.

In obtaining equation (8.4), we have used the transition of the integral with infinite limits for the entire domain ζ_i to the integral on the interface ζ_{SL} . Indeed, let us assume that the interface ζ_{SL} propagates in the direction of the z -axis (figure 4). Then, the complete interface ζ_i consists of the phase interface ζ_{SL} , which represents the solid/liquid interface of a crystal, and three infinite lines defined by $x \rightarrow +\infty$, $x \rightarrow -\infty$ and $z \rightarrow \infty$. In this case, the integral in equation (8.9) is the sum of the integrals over these lines and over the phase interface,

$$\oint_{\zeta_i} d\zeta_i h(r-r') = \oint_{x \rightarrow \infty} d\zeta_i h(r-r') + \oint_{z \rightarrow \infty} d\zeta_i h(r-r') + \oint_{x \rightarrow -\infty} d\zeta_i h(r-r') + \oint_{\zeta_{SL}} d\zeta_i h(r-r'). \quad (8.13)$$

In this sum, the first and third integrals are equal to zero because the Bessel functions are exponentially damping at infinity. Hence, the integral kernel $h(r-r')$ has the following feature:

$$\int_{\zeta_{SL}} h(r-r') d\zeta_i = -1, \quad (8.14)$$

which will be used in the numerical scheme for obtaining a crystal shape.

(b) Numerical method and modelling algorithm

From the computational viewpoint, the boundary integral method is related to the group of front tracking methods. Even though our equation includes local non-equilibrium terms due to $W = V/V_D$, it has the form of the equation solved numerically by Saito *et al.* [31], whose numerical scheme we use to demonstrate the abilities to model dendrites using the boundary integral.

To construct the numerical scheme, let us consider the interface in the form of a polygonal line having $2N+1$ points r_j with symmetry relative to the z -axis. Every segment $s_j = r_{j+1} - r_j$ of the polygonal line is parametrized by λ as

$$\left. \begin{aligned} r(\lambda) &= \phi_1(\lambda)r_j + \phi_2(\lambda)r_{j+1}, \quad x_j = -x_{-j}, \quad z_{-j} = z_j, \\ \phi_1(\lambda) &= \frac{1-\lambda}{2}, \quad \phi_2 = \frac{1+\lambda}{2}, \quad -1 < \lambda < 1, \quad -N < j < N. \end{aligned} \right\} \quad (8.15)$$

The concentration u and its normal gradient $q = \partial u / \partial n$ are linearly interpolated between segments at the interface,

$$u(\lambda) = \phi_1 u_j + \phi_2 u_{j+1} \quad \text{and} \quad q(\lambda) = \phi_1 q_j + \phi_2 q_{j+1}. \quad (8.16)$$

Now, the integral equation (8.4) can be approximated by the system of linear algebraic equations,

$$\sum_{j=-N}^N G_{ij} q_j = \sum_{j=-N}^N H_{ij} u_j, \quad (8.17)$$

where the matrix elements G_{ij} and H_{ij} are computed by the following expressions:

$$\left. \begin{aligned} G_{ij} &= \frac{|s_j|}{2} \int_{-1}^1 g(r_j + \phi_2 s_j - r_i) \phi_1(\lambda) d\lambda + \frac{|s_{j-1}|}{2} \int_{-1}^1 g(r_j - \phi_1 s_{j-1} - r_i) \phi_2(\lambda) d\lambda \\ \text{and} \quad H_{ij} &= \frac{|s_j|}{2} \int_{-1}^1 h(r_j + \phi_2 s_j - r_i) \phi_1(\lambda) d\lambda + \frac{|s_{j-1}|}{2} \int_{-1}^1 h(r_j - \phi_1 s_{j-1} - r_i) \phi_2(\lambda) d\lambda. \end{aligned} \right\} \quad (8.18)$$

To obtain the diagonal elements H_{ii} , we have to use equation (8.14), from which one obtains

$$H_{ii} = -1 - \sum_{j \neq i}^N H_{ij}. \quad (8.19)$$

Using the Gauss method, the integrals of equation (8.18) are approximated by the following finite sum:

$$\int_{-1}^1 f(x) dx = \sum_{i=-n}^n w_i f(x_i). \quad (8.20)$$

Weight coefficients w_i and abscissae x_i can be found in the tables in [66]. With computations of the matrix elements having $i = j$ and $i = j + 1$, one should take into account that integrands include the Bessel functions with a singularity in the zero point. For example,

$$\int_{-1}^1 f(x) dx = \sum_{i=-n}^n w_i f(x_i). \quad (8.21)$$

For the corresponding matrix elements, we use the Gaussian method of functional integration with the logarithmic singularity

$$\int_0^1 \ln(x) f(x) dx = \sum_{i=0}^n w_i f(x_i). \quad (8.22)$$

The weight coefficients w_i and the abscissae of equation (8.22) are also given in [66].

Using the numerical scheme (8.15)–(8.22), one can model the formation of the steady dendritic pattern using the following algorithm:

- the solid/liquid interface is chosen initially as a polygonal line that passes through the points $r_{-N}, \dots, 0, \dots, r_N$;
- the initial value of the normal velocity for these points is W_i ;
- the matrix elements G_{ij} and H_{ij} are calculated by equation (8.18);
- the concentrations in the nodes of the polygonal line, $u_i = C_i(r_i) - C_{l\infty}$, are calculated using the undercooling balance (9.2), which takes an isothermal approximation into account;
- in the solution of the system of linear equations (8.17), the values of a normal concentration gradient, q_i , are obtained;
- the mass balance (8.3) allows us to compute the new values of the velocity W_i of the interface and to choose the new value of the velocity W_0 for the moving reference frame;
- moving every node in the normal direction on the small distance $W_i \delta t$, one obtains the next position of the nodes and entire polygonal line, i.e. the interface;
- at every point r_i , the curvature is calculated as being inversely proportional to the radius of a circle which passes through this and two neighbouring points; the normal to the interface is chosen along the radius of this circle.

A convergence to the expected approximated solution of equation (8.4) is a special problem for this investigation. Here, it is merely expected that the above-described algorithm and computational scheme provide the convergence to the quasi-stationary shape of a pattern with a constant interface velocity. The described algorithm does not model a process of growth; rather, it just represents iterations to the quasi-stationary dendritic configuration. In this iterative process, the convergence essentially depends on the initial configuration of the interface, the parameter δt and the distance δr between the nodes of the polygonal line.¹ Indeed, δt and δr depend on the length $l_D = D_C/V_D$, the diffusion length ℓ and the capillary length d_0 ,

$$\ell = \frac{2\sqrt{1-W^2}}{W} \quad \text{and} \quad d_0 = \frac{\Gamma k_0}{(k_0 - 1)C_{l\infty}m}. \quad (8.23)$$

The diffusion length ℓ defines the thickness of the concentration profile, the concentration gradient and the characteristic scale of the steady pattern. Therefore, to adequately predict the

¹We have provided the algorithm which does not lead to different steady patterns due to different initial configurations of the interface. But the duration of convergence to the final steady pattern, indeed, depends strongly on the initial configuration.

Table 2. Material parameters of the alloying mixture Cu-Ni.

| parameter | | | value |
|---|---------------|------------------------------|----------------------|
| nominal concentration | $C_{l\infty}$ | at. % | 70 |
| melting temperature of Ni | T_f | K | 1726 |
| slope of equilibrium liquidus | m | K/at. % | -43.8 |
| equilibrium distribution coefficient | k_0 | — | 0.81 |
| diffusion coefficient of Ni in the melt | D_C | $\text{m}^2 \text{s}^{-1}$ | 3×10^{-9} |
| diffusion speed in the melt | V_D | m s^{-1} | 20 |
| diffusion speed at the interface | V_{DI} | m s^{-1} | 19 |
| growth kinetic coefficient | μ_k | $\text{m (s}^{-1} \text{K)}$ | 0.24 |
| Gibbs–Thomson coefficient | Γ | K · m | 1.3×10^{-7} |

dendritic pattern, one has to use the inequality $\delta r \ll \ell$. Another limitation comes from the Gibbs–Thomson condition according to which the capillary length defines an action of surface energy for $\delta r > d_0$. Thus, the distance between nodes is limited by the double inequality $d_0 < \delta r \ll \ell$.

9. Pattern selection

The numerical scheme and algorithm formulated in §8 for the boundary integral calculation allow us to study the influence of material parameters and the driving force (undercooling, supersaturation) on the selected quasi-stationary pattern that should appear after the pattern's temporal evolution. In this work, we demonstrate how the shape of the dendrite depends on the anisotropy of the surface energy and the kinetics of atomic attachment. In addition to this, we shall demonstrate an instability of the Ivantsov analytical solution [40,46] and show that undercooling may be high enough to provide a transition from the non-planar cellular–dendritic front.

The two-dimensional computational domain, in which we simulate convergence to the quasi-stationary dendrite growth (§8), is measured and shown below in units of $h_D = D_C/V_D$. For the modelling of dendrite formation under constant temperature, we have chosen a Cu-Ni binary alloy with the material parameters given in table 2. In search of the steady-state shape, we quantitatively evaluate the dendrite tip radius $R(z) = \rho/2$ and dendrite tip velocity $W(z) = V(z)/V_D$ depending on the dimensionless coordinate z measured in units $h_D = D_C/V_D$.

(a) Selection of dendritic shape

Figure 5 shows the influence of anisotropy on the shape of the dendrite. It can be clearly seen that with the decrease in anisotropy of the surface energy the dendrite becomes thicker and the secondary branching comes closer to the dendrite tip (figure 5a–c). And conversely, the amplitude of the side-branches decreases with the increase in the capillary anisotropy α_d . This effect is known from the experiments of Glicksman and co-workers [93,94].

With the lowest anisotropy (figure 5d), the tip radius oscillates in space, exhibiting a non-constant value. The stationary shape, in this case, does not exist even if the kinetic anisotropy is small but not zero. This example demonstrates that, with the small anisotropy of the surface energy and the relatively small undercooling, the kinetic anisotropy does not compensate the beginning of tip splitting.

As a whole, the steady-state dendrites shown in figure 5 differ significantly from the smooth parabolic solutions of Ivantsov. They exhibit branched patterns, which should appear due to noise imposed along the directions with a maximal value of the anisotropy [95,96]—in our case, this is the initially established parabolic contour. Because we did not use subroutines which smooth the computational noise, one can suppose that, in the present calculations, noise may

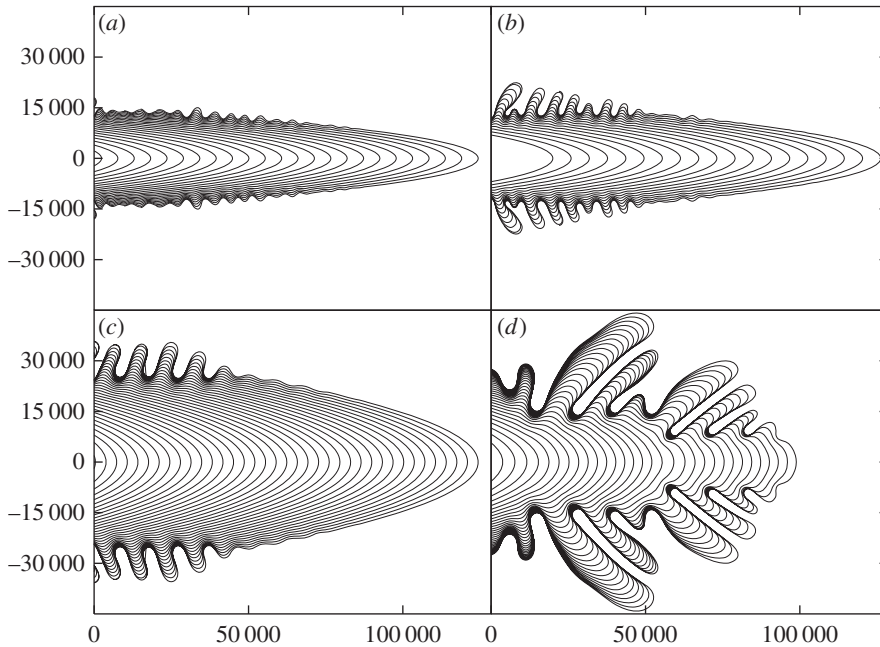


Figure 5. Stroboscopic plots of solidification front positions which show the effect of anisotropy on the dendrite shape selection. Calculations have been made for constant undercooling, $\Delta T = 23$ K, constant kinetic anisotropy, $\alpha_\beta = 0.07$, and various anisotropies of the interfacial energy α_d (stiffness): (a) -0.100 , (b) -0.085 , (c) -0.055 , (d) -0.040 .

come from the grid's discretization and summarizing irregularities arising from the competing side-branches [31]. With the highly discretizing grid, one can expect that the solution will be smoothed when needle-like growing forms are obtained. In this case, reproducing side-branching will be possible by introducing the fluctuation *via* thermodynamic noise which can be taken into account by the additional term to the transport flux (thermal or chemical diffusion flux).

(b) Instability of the Ivantsov solution, tip splitting and fractal formation

Figure 6a clearly demonstrates that anisotropy of the surface energy provides a constant velocity and steady tip radius. This result completely confirms one of the main outcomes of the solvability and boundary integral theories developed for the selection criterion and shows that the isotropic Ivantsov solution for a needle-like dendrite [70,71] is unsteady [40,46]. However, the value of the stiffness of the surface energy α_d should be large enough to preserve the steadily growing dendrite tip. Figure 5d shows that, with a very small value of stiffness, the tip of the dendrite has not found its steady form (within the same size of computational domain as in figure 5a–c) and side-branching has already occurred in the vicinity of the tip. At exactly zero value of the anisotropy, the dendrite tip cannot find and select its constant velocity and the tip radius (figure 6b). We observe that the tip splits with branching that, quantitatively, results in spatially non-monotonic behaviour of the velocity W and tip radius R (figure 7). This non-monotonic behaviour of the velocity with the observed tip splitting exists in the formation of six- or threefold symmetrical patterns induced in ferroelectrics [23] as well as in the formation of fractals [97,98].

(c) Morphological transition at high growth rate

Another effect, which may be demonstrated in applications of the boundary integral theory, is well known as a transition from planar to non-planar growth morphology and vice versa [99]. Here, we demonstrate a transition from the cellular–dendritic pattern to the planar front at high

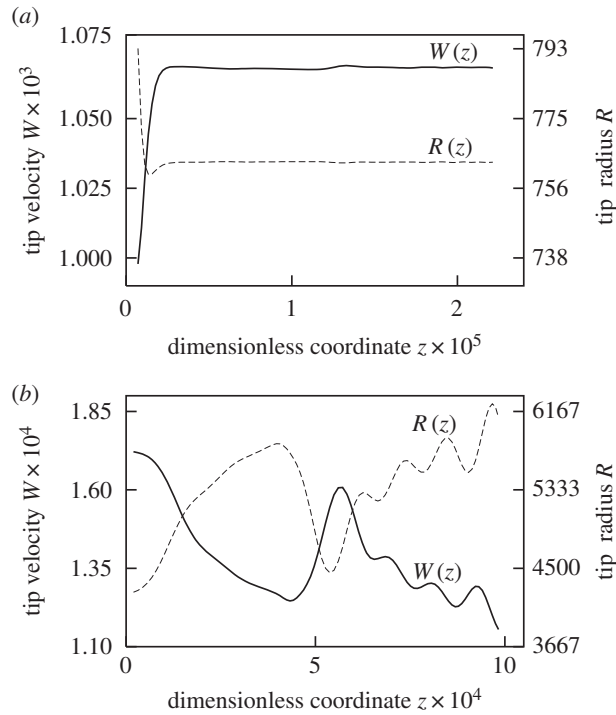


Figure 6. Dendrite tip velocity $W(z) = V(z)/V_D$ and dendrite tip radius $R(z)$ depending on the dimensionless coordinate z measured in units $h_D = D/V_D$. Calculations have been made for constant undercooling, $\Delta T = 23$ K, zero kinetic anisotropy, $\alpha_\beta = 0$, and two values of the anisotropy of the interfacial energy α_d (stiffness): (a) -0.145 and (b) -0.0 .

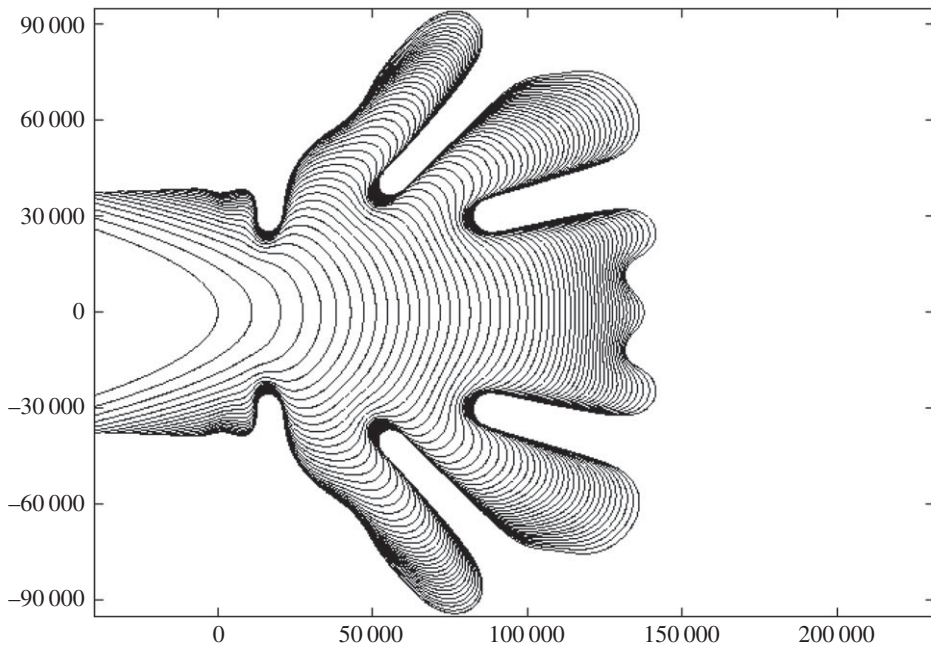


Figure 7. Tip instability in the isotropic case $\alpha_d = 0$ and $\alpha_\beta = 0$. Undercooling is $\Delta T = 23$ K. The size of the computational domain is given in units $h_D = D/V_D$.

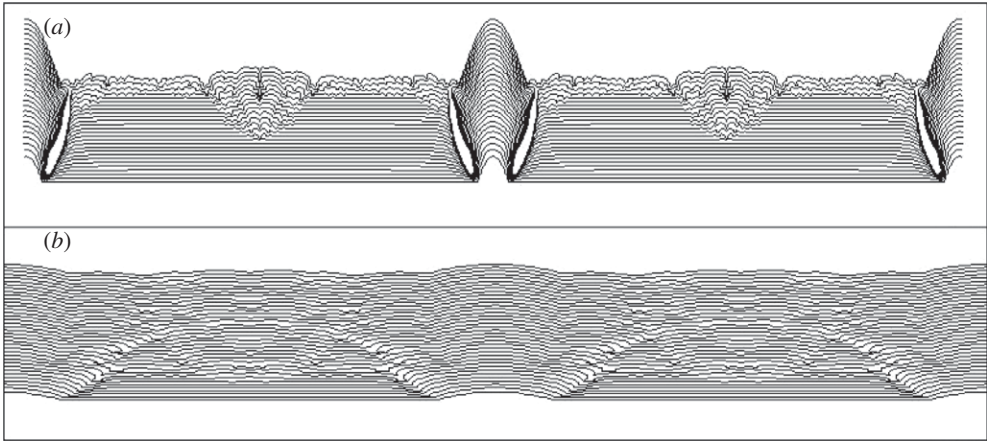


Figure 8. Transition from a non-planar to a planar solid/liquid interface with the increase in undercooling. Calculations have been made for constant kinetic anisotropy, $\alpha_\beta = 0.07$, constant anisotropy of the interfacial energy $\alpha_d = 0.1$ and for two different undercoolings, ΔT : (a) -35 K and (b) -40 K.

growth rate, which was observed experimentally [83,84,100], predicted theoretically [101] and shown in computational simulations [85–87,102]. We qualitatively and quantitatively describe the transition occurring in isothermal rapid solidification of the binary Cu-Ni alloy melt; see the material parameters in table 2 (which are similar to those in [103], where the transition was modelled using mushy zone equations with a cellular automata algorithm).

The results of the present numerical simulations predict cellular–dendritic patterns (figure 8a) which disappear and transform to the planar front (figure 8b) with an increase in undercooling $\Delta T = T_Q \Delta$. As in natural and numerical experiments [83–87,100,102,103], cellular–dendritic structures gradually disappear with the appearance of planar-grained forms or macroscopically smooth planar interfaces, forming a ‘structureless’ example of a pattern.

The transition to a planar front in a rapidly solidifying isothermal sample occurs if the phase interface reaches the velocity of absolute chemical stability [104,105]. The two first curves for V and R shown in figure 9 are given by the model predictions from [106] applied to the dendritic solidification of the Cu-Ni melt under constant temperature. With the increase in undercooling, the tip velocity V and tip radius R gradually increase and decrease, respectively. The model [106] predicts that, in close proximity to critical undercooling ΔT_{CR} , the radius R has a minimum and goes to infinity, which shows the transition to the planar interface (figure 9b). This occurs due to the drastic decrease in the solute boundary layer up to the value of its thickness comparable to the capillary length [104,105]—the scale which stabilizes the planar front. At $\Delta T = \Delta T_{CR}$, the velocity degenerates into a straight line and merges with the velocity

$$W_A \equiv W = \frac{m_v D_C (k_v - 1) C_{l\infty}}{\Gamma k_v^2},$$

for absolute chemical stability (curve 3 in figure 9a). The velocity W for $\Delta T \geq \Delta T_{CR}$ is calculated as [107]

$$W = \frac{\mu_k}{V_D} (\Delta T - \Delta T_{CR}), \quad \Delta T_{CR} = \left(m - \frac{m_v}{k_v} \right) C_{l\infty}, \quad (9.1)$$

where the non-equilibrium solute redistribution function k_v and liquidus slope m_v are given by equations (3.3) and (3.5), respectively. The total undercooling ΔT at the planar interface is given by

$$\Delta T = \Delta T_C + \Delta T_N + \Delta T_K, \quad (9.2)$$

with $\Delta T_C = m_v (C_i - C_{l\infty})$ the solutal undercooling, $\Delta T_N = (m - m_v) C_{l\infty}$ the undercooling due to the change in the equilibrium liquidus slope m to the non-equilibrium liquidus slope m_v ,

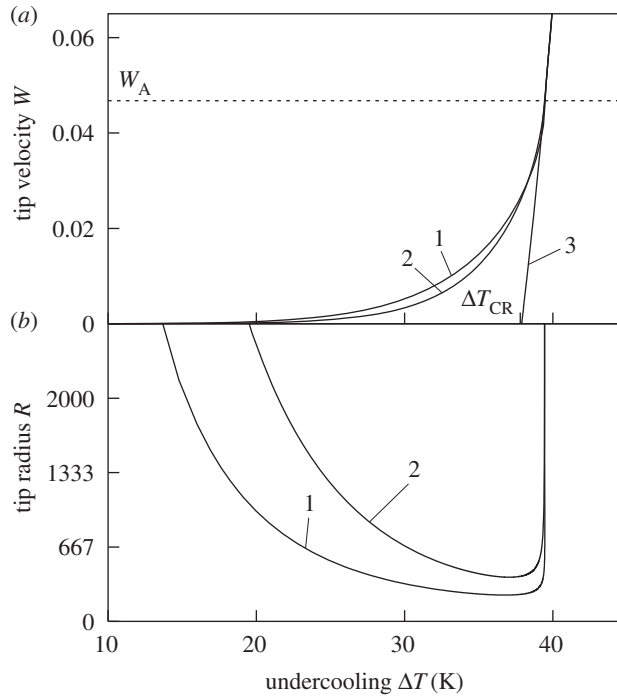


Figure 9. Theoretical predictions given by the model [107] for the dimensionless velocity $W(\Delta T) = V(\Delta T)/V_D$ and tip radius $R(\Delta T)$ measured in units D_C/V_D . Curves present the growth of Ni-Cu dendrites with $\alpha_d = 0.115$ (1) and $\alpha_d = 0.055$ (2). The flat interface (3) starts to grow with $R \rightarrow \infty$ at critical undercooling ΔT_{CR} and velocity $W_A = V_A/V_D$ of the absolute chemical stability.

and $\Delta T_K = V/\mu_k$ the undercooling which is necessary to attach atoms to the interface. By ΔT_{CR} , we denote the critical undercooling above which the steady-state growth of the planar interface becomes possible.

Calculations by equations (9.1) and (9.2) show that the critical undercooling for the beginning of the planar interface growth is $\Delta T_{CR} \approx 38$ K. From the results of the numerical simulation (figure 8), one can see that the transition from the non-planar to the planar interface proceeds; namely, in the range of $\Delta T = 35$ – 40 K, which includes this predicted value of the undercooling ΔT_{CR} . Therefore, the present modelling based on the boundary integral theory gives the quantitatively correct interface velocity, as predicted by the sharp interface model [106] based on the solvability criterion for the selected growth mode of the dendrite.

10. Conclusion

The review paper presents analytical and numerical solutions of a Stefan-type thermo-diffusion problem formulated in terms of a single integro-differential equation for the interface function. The previously known results for parabolic heat and mass transfer are detailed and generalized for rapid phase transition processes accounting for the hyperbolic mass transfer for solute diffusion. The generalized integro-differential equation for the transient interface function contains exhaustive information concerning different peculiarities of interface propagation as well as the structural transformations and growing shapes met in the phase transition processes.

The formulated boundary integral equation contains the previously known growing shapes of dendrites obtained by Ivantsov [70,71] and Horvay & Cahn [79] for local equilibrium steady-state solidification regimes (parabolic equation for heat transfer). In the case of rapid solidification processes, when the transport of particles is described by the hyperbolic equation, the boundary

integral equation leads to the steady-state solutions with the infinite rotational symmetry obtained in [73]. If we are dealing with the finite rotational symmetry of an elliptical paraboloid, the solution for the interface function gives the steady-state solution described in [68] for the case of hyperbolic mass transfer, which includes previously known solutions [70–73,79–81] as limiting cases.

In the limit of large Péclet numbers, $P_T \rightarrow \infty$ and $P_C \rightarrow \infty$, the boundary integral gives semi-spherical solutions for the solid/liquid interface in the vicinity of the dendrite tip. These solutions predict a globular form deformed in the direction of anisotropy strength or a smooth globe in the isotropic case. A qualitative similarity between the boundary integral solution describing globular tips of dendrites and the results of phase-field modelling of globular crystals has been shown for anisotropic and isotropic shapes growing at high growth rates.

In the numerical modelling, we have illustrated the flexibility of the boundary integral theory in reproducing various effects in dendritic growth:

- selection of the dendrite tip velocity and tip radius;
- morphological instability of a smooth parabolic ‘crystal/liquid’ interface with secondary branching propagation along the dendrite surface;
- influence of the interfacial anisotropy on dendrite tip stability with regard to its splitting and the appearance of fractal shapes of crystals;
- transition from cellular–dendritic structures to the planar front at high growth velocity.

Data accessibility. This article has no additional data.

Authors' contributions. All authors contributed equally to the present review paper.

Competing interests. The authors declare that they have no competing interests.

Funding. This work was supported by the Russian Science Foundation (grant no. 16-11-10095) and the German Space Center Space Management under contract no. 50WM1541.

References

1. Langer JS. 1980 Instabilities and pattern formation in crystal growth. *Rev. Mod. Phys.* **52**, 1–28. (doi:10.1103/RevModPhys.52.1)
2. Pelcé P. 1988 *Dynamics of curved fronts*. Boston, MA: Academic Press.
3. Barrett JW, Garcke H, Nürnberg R. 2012 Numerical computations of faceted pattern formation in snow crystal growth. *Phys. Rev. E* **86**, 011604. (doi:10.1103/PhysRevE.86.011604)
4. Libbrecht K. 2004 *Snowflakes*. Minneapolis, MN: Voyageur Press.
5. Libbrecht KG. 2007 The formation of snow crystals. *Am. Sci.* **95**, 52–59. (doi:10.1511/2007.63.52)
6. Sethian JA, Strain J. 1992 Crystal growth and dendritic solidification. *J. Comp. Phys.* **98**, 231–253. (doi:10.1016/0021-9991(92)90140-T)
7. Chung CA, Worster MG. 2002 Steady-state chimneys in a mushy layer. *J. Fluid Mech.* **455**, 387–411. (doi:10.1017/S0022112001007558)
8. Alexandrov DV, Ivanov AA. 2009 The Stefan problem of solidification of ternary systems in the presence of moving phase transition regions. *J. Exp. Theor. Phys.* **108**, 821–829. (doi:10.1134/S1063776109050100)
9. Alexandrova IV, Alexandrov DV, Aseev DL, Bulitcheva SV. 2009 Mushy layer formation during solidification of binary alloys from a cooled wall: the role of boundary conditions. *Acta Phys. Pol. A* **115**, 791–794. (doi:10.12693/APhysPolA.115.791)
10. Lee D, Alexandrov D, Huang H-N. 2010 Numerical modeling of one-dimensional binary solidification—the classical two-phase Stefan problem. *Int. J. Pure Appl. Math.* **58**, 381–416. (doi: 10.4208/nmtma.2012.m1029)
11. Lee D, Alexandrov D, Huang H-N. 2012 Numerical modeling of one-dimensional binary solidification with a mushy layer evolution. *Numer. Math. Theor. Methods Appl.* **5**, 157–185. (doi:10.4208/nmtma.2012.m1029)

12. Alexandrov DV, Malygin AP. 2013 Transient nucleation kinetics of crystal growth at the intermediate stage of bulk phase transitions. *J. Phys. A Math. Theor.* **46**, 455101. (doi:10.1088/1751-8113/46/45/455101)
13. Elder KLM, Seymour M, Lee M, Hilke M, Provatas N. 2018 Two-component structural phase- field crystal models for graphene symmetries. *Phil. Trans. R. Soc. A* **376**, 20170211. (doi:10.1098/rsta.2017.0211)
14. Wang N, Kocher G, Provatas N. 2018 A phase-field-crystal alloy model for late-stage solidification studies involving the interaction of solid, liquid and gas phases. *Phil. Trans. R. Soc. A* **376**, 20170212. (doi:10.1098/rsta.2017.0212)
15. Makoveeva EV, Alexandrov DV. 2018 A complete analytical solution of the Fokker–Planck and balance equations for nucleation and growth of crystals. *Phil. Trans. R. Soc. A* **376**, 20170327. (doi:10.1098/rsta.2017.0327)
16. Alexandrov DV, Bashkirtseva IA, Ryashko LB. 2018 Nonlinear dynamics of mushy layers induced by external stochastic fluctuations. *Phil. Trans. R. Soc. A* **376**, 201700216. (doi:10.1098/rsta.2017.0216)
17. Alexandrov DV, Ivanov AA, Alexandrova IV. 2018 Analytical solutions of mushy layer equations describing directional solidification in the presence of nucleation. *Phil. Trans. R. Soc. A* **376**, 20170217. (doi:10.1098/rsta.2017.0217)
18. Herlach DM, Simons D, Pichon P-Y. 2018 Crystal growth kinetics in undercooled melts of pure Ge, Si and Ge–Si alloys. *Phil. Trans. R. Soc. A* **376**, 20170205. (doi:10.1098/rsta.2017.0205)
19. Galenko PK, Nizovtseva IG, Reuther K, Rettenmayr M. 2018 Kinetic transition in the order–disorder transformation at a solid/liquid interface. *Phil. Trans. R. Soc. A* **376**, 20170207. (doi:10.1098/rsta.2017.0207)
20. Alexandrov DV, Galenko PK, Toropova LV. 2018 Thermo-solutal and kinetic modes of stable dendritic growth with different symmetries of crystalline anisotropy in the presence of convection. *Phil. Trans. R. Soc. A* **376**, 20170215. (doi:10.1098/rsta.2017.0215)
21. Jou D, Galenko PK. 2018 Coarse-graining for fast dynamics of order parameters in the phase-field model. *Phil. Trans. R. Soc. A* **376**, 20170203. (doi:10.1098/rsta.2017.0203)
22. Nizovtseva IG, Galenko PK. 2018 Traveling-wave amplitudes as solutions of the phase field crystal equation. *Phil. Trans. R. Soc. A* **376**, 20170202. (doi:10.1098/rsta.2017.0202)
23. Shur VYa, Akhmatkhanov AR. 2018 Domain instabilities and dendrite domain growth in uniaxial ferroelectrics. *Phil. Trans. R. Soc. A* **376**, 20170204. (doi:10.1098/rsta.2017.0204)
24. Kao A, Gao J, Pericleous K. 2018 Thermoelectric magnetohydrodynamic effects on the crystal growth rate of undercooled Ni dendrites. *Phil. Trans. R. Soc. A* **376**, 20170206. (doi:10.1098/rsta.2017.0206)
25. Gao J. 2018 A model for free growth of a lamellar eutectic dendrite with an incident flow. *Phil. Trans. R. Soc. A* **376**, 20170209. (doi:10.1098/rsta.2017.0209)
26. Cool T, Voorhees PW. 2018 Dendrite fragmentation: an experiment-driven simulation. *Phil. Trans. R. Soc. A* **376**, 20170213. (doi:10.1098/rsta.2017.0213)
27. Nash GE. 1974 Capillary-limited, steady state dendritic growth. Part I. Theoretical development. NRL Report 7679, May 1974.
28. Nash GE, Glicksman ME. 1974 Capillary-limited steady-state dendritic growth—I. Theoretical development. *Acta Metall.* **22**, 1283–1290. (doi:10.1016/0001-6160(74)90141-2)
29. Langer JS, Turski LA. 1977 Studies in the theory of interfacial stability—I. Stationary symmetric model. *Acta Metall.* **25**, 1113–1119. (doi:10.1016/0001-6160(77)90199-7)
30. Langer JS. 1977 Studies in the theory of interfacial stability—II. Moving symmetric model. *Acta Metall.* **25**, 1121–1137. (doi:10.1016/0001-6160(77)90200-0)
31. Saito Y, Goldbeck-Wood G, Müller-Krumbhaar H. 1988 Numerical simulation of dendritic growth. *Phys. Rev. A* **38**, 2148–2157. (doi:10.1103/PhysRevA.38.2148)
32. Hou TY, Lowengrub JS, Shelley MJ. 2001 Boundary integral methods for multicomponent fluids and multiphase materials. *J. Comput. Phys.* **169**, 302–362. (doi:10.1006/jcph.2000.6626)
33. Alexandrov DV, Galenko PK. 2017 Boundary integral approach for propagating interfaces in a binary non-isothermal mixture. *Physica A* **469**, 420–428. (doi:10.1016/j.physa.2016.11.062)
34. Pelce P, Pomeau Y. 1986 Dendrites in the small undercooling limit. *Stud. Appl. Math.* **74**, 245–258. (doi:10.1002/sapm1986743245)
35. Ben Amar M, Pomeau Y. 1986 Theory of dendritic growth in a weakly undercooled melt. *Europhys. Lett.* **2**, 307–314. (doi:10.1209/0295-5075/2/4/008)

36. Ben Amar M. 1988 Theory of needle-crystal. *Physica D* **31**, 409–423. (doi:10.1016/0167-2789(88)90006-1)
37. Barbieri A, Hong DC, Langer JS. 1987 Velocity selection in the symmetric model of dendritic crystal growth. *Phys. Rev. A* **35**, 1802–1808. (doi:10.1103/PhysRevA.35.1802)
38. Barbieri A, Langer JS. 1989 Predictions of dendritic growth rates in the linearized solvability theory. *Phys. Rev. A* **39**, 5314–5325. (doi:10.1103/PhysRevA.39.5314)
39. Barber MN, Barbieri A, Langer JS. 1987 Dynamics of dendritic sidebranching in the two-dimensional symmetric model of solidification. *Phys. Rev. A* **36**, 3340–3349. (doi:10.1103/PhysRevA.36.3340)
40. Brener EA, Mel'nikov VA. 1991 Pattern selection in two-dimensional dendritic growth. *Adv. Phys.* **40**, 53–97. (doi:10.1080/00018739100101472)
41. Barbieri A. 1987 Velocity selection at large undercooling in a two-dimensional nonlocal model of solidification. *Phys. Rev. A* **36**, 5353–5358. (doi:10.1103/PhysRevA.36.5353)
42. Brener EA, Mel'nikov VA. 1990 Two-dimensional dendritic growth at arbitrary Peclet number. *J. Phys. France* **51**, 157–166. (doi:10.1051/jphys:01990005102015700)
43. Brener EA. 1990 Effects of surface energy and kinetics on the growth of needle-like dendrites. *J. Cryst. Growth* **99**, 165–170. (doi:10.1016/0022-0248(90)90505-F)
44. Alexandrov DV, Galenko PK. 2013 Selection criterion for the growing dendritic tip at the inner core boundary. *J. Phys. A Math. Theor.* **46**, 195101. (doi:10.1088/1751-8113/46/19/195101)
45. Alexandrov DV, Galenko PK. 2017 Dendritic growth with the six-fold symmetry: theoretical predictions and experimental verification. *J. Phys. Chem. Solids* **108**, 98–103. (doi:10.1016/j.jpcs.2017.04.016)
46. Kessler DA, Koplik J, Levine H. 1988 Pattern selection in fingered growth phenomena. *Adv. Phys.* **37**, 255–339. (doi:10.1080/00018738800101379)
47. Galenko PK, Danilov DA. 1997 Local nonequilibrium effect on rapid dendritic growth in a binary alloy melt. *Phys. Lett. A* **235**, 271–280. (doi:10.1016/S0375-9601(97)00562-8)
48. Alexandrov DV, Danilov DA, Galenko PK. 2016 Selection criterion of a stable dendrite growth in rapid solidification. *Int. J. Heat Mass Transf.* **101**, 789–799. (doi:10.1016/j.ijheatmasstransfer.2016.05.085)
49. Flemings MC. 1974 *Solidification processing*. New York, NY: McGraw-Hill.
50. Lyubov BYa. 1975 *Theory of crystallization in large volumes*. Moscow, Russia: Nauka.
51. Gupta SC. 2003 *Classical Stefan problem*. Amsterdam, The Netherlands: Elsevier.
52. Alexandrov DV, Nizovtseva IG, Malygin AP, Huang H-N, Lee D. 2008 Unidirectional solidification of binary melts from a cooled boundary: analytical solutions of a nonlinear diffusion-limited problem. *J. Phys. Condens. Matter* **20**, 114105. (doi:10.1088/0953-8984/20/11/114105)
53. Alexandrov DV, Ivanov AA. 2009 Solidification of a ternary melt from a cooled boundary, or nonlinear dynamics of mushy layers. *Int. J. Heat Mass Transf.* **52**, 4807–4811. (doi:10.1016/j.ijheatmasstransfer.2009.05.029)
54. Ben Amar M. 1990 Dendritic growth rate at arbitrary undercooling. *Phys. Rev. A* **41**, 2080–2092. (doi:10.1103/PhysRevA.41.2080)
55. Conti M. 2000 Thermal and chemical diffusion in the rapid solidification of binary alloys. *Phys. Rev. E* **61**, 642–650. (doi:10.1103/PhysRevE.61.642)
56. Alexandrov DV, Galenko PK. 2015 Thermo-solutal and kinetic regimes of an anisotropic dendrite growing under forced convective flow. *Phys. Chem. Chem. Phys.* **17**, 19149–19161. (doi:10.1039/c5cp03018h)
57. Cogswell DA, Carter WC. 2011 Thermodynamic phase-field model for microstructure with multiple components and phases: the possibility of metastable phases. *Phys. Rev. E* **83**, 061602-1–13. (doi:10.1103/PhysRevE.83.061602)
58. Choudhury A, Nestler B, Plapp M. 2012 Grand-potential formulation for multicomponent phase transformations combined with thin-interface asymptotics of the double-obstacle potential. *Phys. Rev. E* **85**, 021602-1–16. (doi:10.1103/PhysRevE.85.021602)
59. Herlach D. 1994 Non-equilibrium solidification of undercooled metallic melts. *Mater. Sci. Eng. R.* **12**, 177–272. (doi:10.1016/0927-796X(94)90011-6)
60. Galenko PK, Herlach DM. 2006 Diffusionless crystal growth in rapidly solidifying eutectic systems. *Phys. Rev. Lett.* **96**, 150602. (doi:10.1103/PhysRevLett.96.150602)

61. Yang Y, Humadi H, Buta D, Laird BB, Sun D, Hoyt JJ, Asta M. 2011 Atomistic simulations of nonequilibrium crystal-growth kinetics from alloy melts. *Phys. Rev. Lett.* **107**, 025505. (doi:10.1103/PhysRevLett.107.025505)
62. Jou D, Galenko PK. 2013 Coarse graining for the phase-field model of fast phase transitions. *Phys. Rev. E* **88**, 042151. (doi:10.1103/PhysRevE.88.042151)
63. Galenko P. 2007 Solute trapping and diffusionless solidification in a binary system. *Phys. Rev. E* **76**, 031606. (doi:10.1103/physreve.76.031606)
64. Galenko P. 2002 Extended thermodynamical analysis of a motion of the solid-liquid interface in a rapidly solidifying alloy. *Phys. Rev. B* **65**, 144103. (doi:10.1103/physrevb.65.144103)
65. Morse PM, Feshbach H. 1953 *Methods of theoretical physics*. New York, NY: McGraw-Hill.
66. Abramowitz M, Stegun IA. 1972 *Handbook of mathematical functions*. New York, NY: Dover Publishing.
67. Gradshteyn IS, Ryzhik IM. 2007 *Tables of integrals, series, and products*. New York, NY: Academic Press.
68. Galenko PK, Danilov DA. 2000 Steady-state shapes of growing crystals in the field of local nonequilibrium diffusion. *Phys. Lett. A* **272**, 207–217. (doi:10.1016/S0375-9601(00)00417-5)
69. Alexandrov DV, Galenko PK. 2017 Selected mode for rapidly growing needle-like dendrite controlled by heat and mass transport. *Acta Mater.* **137**, 64–70. (doi:10.1016/j.actamat.2017.07.022)
70. Ivantsov GP. 1947 Temperature field around spherical, cylinder and needle-like dendrite growing in supercooled melt. *Dokl. Akad. Nauk SSSR* **58**, 567–569.
71. Ivantsov GP. 1952 On a growth of spherical and needle-like crystals of a binary alloy. *Dokl. Akad. Nauk SSSR* **83**, 573–575.
72. Alexandrov DV, Galenko PK. 2014 Dendrite growth under forced convection: analysis methods and experimental tests. *Phys. Usp.* **57**, 771–786. (doi:10.3367/UFNr.0184.201408b.0833)
73. Galenko PK, Danilov DA, Alexandrov DV. 2015 Solute redistribution around crystal shapes growing under hyperbolic mass transport. *Int. J. Heat Mass Transf.* **89**, 1054–1060. (doi:10.1016/j.ijheatmasstransfer.2015.06.011)
74. Ben-Jacob E, Goldenfeld N, Langer JS, Schön G. 1984 Boundary-layer model of pattern formation in solidification. *Phys. Rev. A* **29**, 330–340. (doi:10.1103/PhysRevA.29.330)
75. Teraoka Y, Saito A, Okawa S. 2002 Ice crystal growth in supercooled solution. *Int. J. Refrig.* **25**, 218–225. (doi:10.1016/S0140-7007(01)00082-2)
76. Yoshizaki I, Ishikawa T, Adachi S, Yokoyama E, Furukawa Y. 2012 Precise measurements of dendritic growth of ice crystals in microgravity. *Microgravity Sci. Technol.* **24**, 245–253. (doi:10.1007/s12217-012-9306-9)
77. Nersisyan HH, Kim DY, Yoo B, Kang W, Han B, Lee J. 2016 Experimental growth of new 6-fold symmetry patterned microcrystals of AlN: equilibrium structures and growth mechanism. *Cryst. Growth Des.* **16**, 5305–5311. (doi:10.1021/acs.cgd.6b00829)
78. Shur VYa, Akhmatkhanov AR, Pelegova EV. 2016 Self-organizing formation of dendrite domain structures in lithium niobate and lithium tantalate crystals. *Ferroelectrics* **500**, 76–89. (doi:10.1080/00150193.2016.1229114)
79. Horvay G, Cahn JW. 1961 Dendritic and spheroidal growth. *Acta Metall.* **9**, 695–705. (doi:10.1016/0001-6160(61)90008-6)
80. McFadden GB, Coriell SR, Sekerka RF. 2000 Analytic solution for a non-axisymmetric isothermal dendrite. *J. Cryst. Growth* **208**, 726–745. (doi:10.1016/S0022-0248(99)00478-9)
81. Titova EA, Alexandrov DV, Galenko PK. 2017 Boundary integral approach for elliptical dendritic paraboloid as a form of growing crystals. *IOP Conf. Ser. Mater. Sci. Eng.* **192**, 012025. (doi:10.1088/1757-899X/192/1/012025)
82. Hartmann H, Galenko PK, Holland-Moritz D, Kolbe M, Herlach DM, Shuleshova O. 2008 Nonequilibrium solidification in undercooled Ti₄₅Al₅₅ melts. *J. Appl. Phys.* **103**, 073509–1–9. (doi:10.1063/1.2903920)
83. Ovsienko DE, Alfintsev GA, Maslov VV. 1974 Kinetics and shape of crystal growth from the melt for substances with low L/kT values. *J. Cryst. Growth* **26**, 233–238. (doi:10.1016/0022-0248(74)90251-6)
84. Fedorov OP. 2010 *Processes of crystal growth: kinetics, shape formation, inhomogeneities*. Kiev, Ukraine: Naukova Dumka.

85. Umantsev AR, Vinogradov VV, Borisov VT. 1986 Modeling the evolution of a dendritic structure. *Sov. Phys. Crystallogr.* **31**, 596–599.
86. Galenko PK, Zhuravlev VA. 1994 *Physics of dendrites*. Singapore: World Scientific.
87. Danilov D, Nestler B. 2004 Dendritic to globular morphology transition in ternary alloy solidification. *Phys. Rev. Lett.* **93**, 215501-1–4. (doi:10.1103/PhysRevLett.93.215501)
88. Karma A, Rappel W-J. 1999 Phase-field model of dendritic sidebranching with thermal noise. *Phys. Rev. E* **60**, 3614–3625. (doi: 1063-651X/99/60(4)/3614(12))
89. Galenko PK, Herlach DH. 2006 Fractals, morphological spectrum and complexity of interfacial patterns in non-equilibrium solidification. In *Complexus mundi: emergent patterns in nature* (ed. MM Novak), pp. 199–208. Hackensack, NJ: World Scientific.
90. Provatas N, Elder K. 2010 *Phase-field methods in materials science and engineering*. Weinheim, Germany: Wiley-VCH.
91. Emmerich H. 2003 *The diffuse interface approach in materials science*. Berlin, Germany: Springer.
92. Salhoumi A, Galenko PK. 2016 Gibbs-Thomson condition for the rapidly moving interface in a binary system. *Physica A* **447**, 161–71. (doi:10.1016/j.physa.2015.12.042)
93. Glicksman ME, Schaefer RJ, Ayers JD. 1976 Dendritic growth—a test of theory. *Metall. Trans. A* **7**, 1747–1759. (doi:10.1007/BF03186673)
94. Huang S-C, Glicksman ME. 1981 Overview 12: fundamentals of dendritic solidification—II. Development of sidebranch structure. *Acta Metall.* **29**, 717–734. (doi:10.1016/0001-6160(81)90116-4)
95. Brenner E, Temkin D. 1995 Noise-induced sidebranching in the three-dimensional nonaxisymmetric dendritic growth. *Phys. Rev. E* **51**, 351–359. (doi:10.1103/PhysRevE.51.351)
96. Bisang U, Bilgram JH. 1995 Shape of the tip and the formation of sidebranches of xenon dendrites. *Phys. Rev. Lett.* **75**, 3898–3901. (doi: 10.1103/PhysRevLett.75.3898)
97. Pietronero L, Tosatti E (eds). 1986 *Fractals in physics*. Amsterdam, The Netherlands: Elsevier.
98. Vicsek T. 1992 *Fractal growth phenomena*, 2nd edn. Singapore: World Scientific.
99. Coriell SR, McFadden GB. 1993 Morphological stability. In *Handbook of crystal growth*, vol. 1 (ed. DTJ Hurle), ch. 12, pp. 785–857. Amsterdam, The Netherlands: Elsevier.
100. Ludwig A, Kurz W. 1996 Direct observation of solidification microstructures around absolute stability. *Acta Mater.* **44**, 3643–3654. (doi:10.1016/1359-6454(95)00448-3)
101. Misbach C, Müller-Krumbhaar H, Temkin DE. 1991 Interface structure at large supercooling. *J. Phys. I* **1**, 585–601. (doi:10.1051/jp1:1991154)
102. Gránásy L, Rátkai L, Szállás A, Korbuly B, Tóth GI, Környei L, Pusztai T. 2014 Phase-field modeling of polycrystalline solidification: from needle crystals to spherulites—a review. *Metal. Mater. Trans. A* **45**, 1694–1719. (doi:10.1007/s11661-013-1988-0)
103. Galenko P, Krivilyov M. 1997 Crystal pattern formation under local nonequilibrium solidification. In *Fractal frontiers* (eds M Novak, T Dewey), pp. 411–419. Singapore: World Scientific.
104. Trivedi R, Kurz W. 1986 Morphological stability of a planar interface under rapid solidification conditions. *Acta Metall.* **34**, 1663–1670. (doi:10.1016/0001-6160(86)90112-4)
105. Kurz W, Fisher R. 1989 *Fundamentals of solidification*, 4th edn. Aedermannsdorf, Switzerland: Trans Tech.
106. Galenko PK, Danilov DA, Reuther K, Alexandrov DV, Rettenmayr M, Herlach DM. 2017 Effect of convective flow on stable dendritic growth in rapid solidification of a binary alloy. *J. Cryst. Growth* **457**, 349–355. (doi:10.1016/j.jcrysgro.2016.07.042)
107. Galenko PK, Danilov DA. 2000 Selection of the dynamically stable regime of rapid solidification front motion in an isothermal binary alloy. *J. Cryst. Growth* **216**, 512–536. (doi:10.1016/S0022-0248(00)00338-9)